Supplementary Information for

Single-junction organic solar cells with over 19% efficiency enabled by a refined double-fibril network morphology

Lei Zhu[1,8], Ming Zhang[1,8], Jinqiu Xu[1,8], Chao Li[2], Jun Yan[3]*, Guanqing Zhou[1], Wenkai Zhong[1], Tianyu Hao[1], Jiali Song[2], Xiaonan Xue[1], Zichun Zhou[1], Rui Zeng[1], Haiming Zhu[4], Chun-Chao Chen[5], Roderick C.I. MacKenzie[6], Yecheng Zou[7], Jenny Nelson[3], Yongming Zhang[1,7], Yanming Sun[2]*, Feng Liu[1,7]*

[1]Frontiers Science Center for Transformative Molecules, In-situ Center for Physical Science, and Center of Hydrogen Science, School of Chemistry and Chemical Engineering, Shanghai Jiao Tong University, Shanghai 200240, China.

[2]School of Chemistry, Beihang University, Beijing 100191, China.

[3]Department of Physics, Imperial College London, London SW7 2AZ, UK.

[4]Department of Chemistry, Zhejiang University, Hangzhou, Zhejiang 310027, China.

[5]School of Materials Science and Engineering, Shanghai Jiao Tong University, Shanghai 200240, China.

[6]Department of Engineering, Durham University, Durham DH1 3LE, UK.

[7]State Key Laboratory of Fluorinated Functional Membrane Materials and Dongyue Future Hydrogen Energy Materials Company, Zibo, Shandong 256401, China.

[8]These authors contributed equally: Lei Zhu, Ming Zhang, Jinqiu Xu.

*e-mail: j.yan17@imperial.ac.uk; sunym@buaa.edu.cn; fengliu82@sjtu.edu.cn

Table of Contents

Materials and Methods

Materials

Chloroform (Sigma-Aldrich, ≥99%), methanol (Alfa, 99.8%), acetic acid (Alfa, 99.9%), DIO (Sigma-Aldrich, 98%), 1-CN (TCI, 97%) and 1,4-diiodobenzene (TCI, 98%) were purchased from commercial sources and used without further purification. PM6, PM7, D18, ITIC, IT4F, IDIC, Y6, BTP-eC9, PFN-Br, and PDINN were purchased from Solarmer Material Inc. D18-Cl and PNDIT-F3N were purchased from eFlexPV Limited. PTQ10 was purchased from 1-Material Inc. L8-BO, IDTT-C10-TIC, and PBT1-C-2Cl were designed and synthesized by Yanming Sun's group.

Measurements and instruments

UV–vis absorption spectra were recorded on a Shimadzu spectrometer model UV-1800 with films on the quartz plates at room temperature. Ultraviolet photoelectron spectrometer (UPS) measurement was performed by AXIS ULTRA DLD instrument of Kratos company. The UV light source used is non-monochromatic He I, and the energy of He I light source is 21.22 eV. The basic vacuum of the analysis chamber is 3.0×10^{-8} Torr, and the bias voltage applied during the test is −9 V. Inverse photoemission spectroscopy (IPES) measurement was performed using a customized ULVAC-PHI LEIPS instrument with Bremsstrahlung isochromatic mode. TEM measurements were carried out on a JEOL JEM-1400 (Japan) transmission electron microscope. AFM measurements were performed using a Dimension Icon AFM instrument (Bruker) in the tapping mode. SEM measurements were carried out on a GeminiSEM 500 (ZEISS Co., Germany) scanning electron microscope. The GIWAXS characterization of the thin films was performed at the Advanced Light Source (Lawrence Berkeley National Laboratory) on beamline 7.3.3. The incidence angle was 0.16°, and the beam energy was 10 keV. Samples were prepared under device conditions on the Si/PEDOT:PSS substrates. RSoXS was performed at beamline 11.0.1.2 (ALS, LBNL) with different bean energies. Samples were prepared under device conditions on the Si/PEDOT:PSS substrates, then placed in water and transferred to a silicon nitride window. The scattering signals were collected in a vacuum using a Princeton Instrument-motion tracking enhancement technique (PI-MTE) charge-coupled device (CCD) camera. Polarized resonant X-ray scattering (PSoXS) was performed to elucidate the relative orientation of the components in the active layers.

Device characterization

The current–voltage (*J*–*V*) curves were measured with Keithley 2400 Source under the illumination of AM 1.5 G irradiation (100 mW cm^{-2}) using a 150 W solar simulator (DM-40S3, SAN-EI ELECTRIC, Japan) in a glove box at room temperature. The light intensity was determined by a 2 × 2 cm^2 standardized mono silicon cell (Oriel PN 91150V, Newport, USA.) calibrated by the National Renewable Energy Laboratory (NREL). The external quantum efficiency (EQE) measurement was conducted on a TRACQ-BASIC System using a lock-in amplifier with a monochromator and 500 W xenon lamp. A calibrated silicon detector (PRL-12, Newport, USA) with a known photoresponse was utilized as a reference. The *J*–*V* curves were measured along the reverse scan direction from 1.0 to −0.1 V, yielding identical results. The scan speed and dwell times were fixed at 0.02 V/step and 20 ms, respectively. During the test, an aperture with an area of 3.2 or 10.4 mm^2 is used to calibrate the device area.

Photo-induced force microscope (PiFM)

For tapping PiFM measurements, an IR-neaSCOPE from neaspec was used to map IR absorption via detecting the mechanical response of an AFM cantilever upon sample stimulation by pulsed IR light. In the instrument, a pulsed tunable QCL laser is focused onto a PtIr coated AFM probe via a parabolic mirror, while the microscope is operated in the intermittent contact mode. The readout of the optically induced changes in the sample is performed by providing bimodal excitation of the cantilever and monitoring the response at the second cantilever Eigen-mode, while the first Eigen-mode is used for AFM topography and feedback. Such an active bimodal technique enables reliable tracking of the cantilever resonance, which in turn suppresses mechanically induced artifacts in the PiFM image contrasts. The pulse width of the QCL laser is in the ns range in tapping PiFM operation. The linewidth of the laser is typically about 1 cm^{-1}. The accessible spectral range depends on the selection of central wavelengths when equipping the laser. Up to 4 ranges can be selected and within those ranges, the laser is freely tunable. In this measurement mode, a resolution of ~1 cm^{-1} can be achieved within the tuning range of the laser.

SCLC mobility measurements

The electron-only devices were fabricated with ITO/ZnO/Active layer/ZnO/Ag structures and hole-only devices were fabricated with ITO/PEDOT:PSS/active layer/Au structures. The thickness of the active layer is ~120 nm. The mobilities were extracted using a full drift diffusion model simulation (gpvdm)[1,2] with gaussian type trap states, and the parameters are listed in Supplementary Table 8. Key input parameters are the trap profiles, including the total trap density, trap depth, and the trap state gaussian width, which were estimated using capacitance-frequency measurements as presented in Supplementary Fig. 27. This leads to only two fitting parameters to extract the mobilities, which are the injection barriers (e and h). The fitted curves and the resulting mobility values are shown in Supplementary Fig. 25 and Supplementary Table 9, respectively.

Transient photovoltage (TPV) and photocurrent (TPC) measurements

The background illumination was provided by the LED light source, and pulsed light was provided by an arbitrary wave generator (AFG322C, Tektronix). The photovoltage traces were registered by the oscilloscope (AFG322C, Tektronix). The photocurrent traces were registered with the resistance of 50 Ω, switching open-circuit mode to short-circuit mode. The integrated TPC signal provides a measure of the total charge generated by the LED light source. The exponential fitting was used to process the *V–t* curves measuring from the TPV signal to obtain the lifetime of carriers. The total charge generated by LED was obtained from the integrated TPC signal. Empirically, the differential capacitance values are found to follow the exponential dependence on the open-circuit voltage given by $C = \frac{\Delta Q}{\Delta V_0} = C_0 \exp\left(\gamma V_{\mathrm{oc}}\right) + D$ [C is the differential capacitance (F), ΔQ is the total charge generated by a pulse (C), ΔV_0 is the TPV magnitude (V), C_0 is the exponential capacitance prefactor (F), γ is the capacitance exponential constant (V^{-1}), D is the effectively fixed capacitance (F)], so the charge-carrier density as a function of V_{oc} is given by treating the device as a parallel-plate capacitor and integrating with respect to voltage, as $n = \frac{1}{Aed} \int_{-\infty}^{V_{\mathrm{oc}}} C_0 \exp\left(\gamma V\right) \mathrm{d}V$ [n is the bulk charge-carrier density (m^{-3}), A is the area of the device (m^2), d is the thickness of the active layer (m)].[3] Then, the recombination rate coefficient can be determined, which is defined by $k(n) = \frac{1}{\tau(n) \cdot n}$.

Impedance spectroscopy (IS)

The measurements were carried out by illumination with an AM 1.5G irradiation (100 mW cm^{-2}) using a solar simulator. Impedance spectra were measured for different light intensities at frequencies from 8 MHz to 50 Hz. To measure in V_{oc} conditions, a bias voltage equal to V_{oc}

at each light intensity was applied. A 10 mV AC perturbation is used, and in this case, the excess holes and electrons are generated into the donor HOMO and acceptor LUMO manifolds, then diffuse along with the diode bulk, and eventually recombine. The molecular orbitals spread in energy DoS following the exponential shape, and the occupancy level of the LUMO state is determined by the competition of photo-generation and recombination, which in turn governs the achievable V_{oc}. Recombination resistance (R_{rec}) and chemical capacitance (C_{μ}^{n}) were directly extracted from the low-frequency region. The chemical capacitors determined by IS reflect the capability of the photovoltaic device to accept or release additional charge carriers as the result of the shifting in the quasi-Fermi level. The DoS (g_{n}) is obtained by $C_{\mu}^{n} = Sqg_{\mathrm{n}}(E_{\mathrm{Fn}})$, where S is the device area and q is the elemental charge. A typical exponential shape is seen, and the curves are fitted by $g_{\mathrm{n}}(E_{\mathrm{Fn}}) = \frac{N}{\delta}\exp\left(-\frac{E_{\mathrm{g}} - E_{\mathrm{Fn}}}{\delta}\right)$, where N is the total density per unit volume, E_{g} is the bandgap extracted from the EQE tail, and δ is the broadening of the DoS that describes energetic disorder.

The curves of C_{μ}^{n} and R_{rec} are fitted by $C_{\mu}^{n} = C_0 \exp\left(\frac{\alpha qV}{kT}\right)$ and $R_{\mathrm{rec}} = R_0 \exp\left(-\frac{\beta qV}{kT}\right)$. The density of electrons n is the integration of C_{μ}^{n} to voltage, so the density of electrons n is proportional to $\exp\left(\frac{\alpha qV}{kT}\right)$, that is $n \propto \exp\left(\frac{\alpha qV_{\mathrm{F}}}{kT}\right)$. If one further assumes that the dominant recombination process is mono- or bimolecular, recombination current J_{rec} will be proportional to n or n^2, so $J_{\mathrm{rec}} \propto \exp\left(\frac{\alpha qV}{kT}\right)$ or $J_{\mathrm{rec}} \propto \exp\left(\frac{2\alpha qV}{kT}\right)$. In open-circuit conditions, J_{rec} is phenomenologically modeled as $J_{\mathrm{rec}} = J_0\left[\exp\left(\frac{\alpha qV}{kT}\right) - 1\right]$. Therefore, validation of the recombination law can be reinforced from the experimental relationships between α and β parameters. As for the mono-molecular recombination process, it is derived that $\beta = \alpha$, and for the bimolecular recombination process, $\beta = 2\alpha$. If considering shallow trapped carriers in the exponential tail as the dominant non-geminate loss mechanism, the corresponding recombination current is $J_{\mathrm{rec}} \propto n \cdot n_{\mathrm{t}}$, in which the density of trapped carriers (n_{t}) relates to free carriers (n) by $n_{\mathrm{t}} \propto n^{kT/E_{\mathrm{U}}}$. Then, it is derived that $J_{\mathrm{rec}} \propto n_{\mathrm{t}}^{E_{\mathrm{U}}/kT+1}$, and if $E_{\mathrm{U}} > kT$, then $\beta > 2\alpha$.

Transient absorption spectroscopy (TA)

For femtosecond transient absorption spectroscopy, the fundamental output from Yb:KGW laser (1030 nm, 220 fs Gaussian fit, 100 kHz, Light Conversion Ltd) was separated into two light beams. One was introduced to NOPA (ORPHEUS-N, Light Conversion Ltd) to produce a certain wavelength for pump beam (here we use 550 and 750 nm, 30 fs pulse duration), the other was focused onto a YAG plate to generate white light continuum as the probe beam. The pump and probe overlapped on the sample at a small angle of less than 10°. The transmitted probe light from the sample was collected by a linear CCD array.

Exciton annihilation method

The exciton annihilation method is used to estimate the diffusion length of each neat films[4,5]. The series of fluence dependent decays are globally fit to a rate equation accounting for bimolecular (exciton annihilation) and monomolecular decay pathways, assuming that annihilation destroys both excitons: $\frac{\mathrm{d}n(t)}{\mathrm{d}t} = -kn(t) - \frac{1}{2}\gamma n^2(t)$ (1), which has the following solution: $n(t) = \frac{n(0)e^{-kt}}{1+\frac{\gamma}{2k}n(0)\left(1-e^{-kt}\right)}$ (2), where $n(t)$ is the singlet exciton density as a function of time after the laser excitation, k is the monomolecular decay rate and γ is the singlet-singlet bimolecular exciton annihilation rate. Here the intrinsic monomolecular decay constant, k, is extracted from the dilute neat film under weak laser irradiation (< 1 μJ cm^{-2}). The exciton decays can be well fit by Eq. (2), where the only free parameter is the bimolecular rate constant. The bimolecular rate constant is then used $D = \frac{\gamma}{8\pi R}$ to determine the 3D exciton diffusion coefficient, where D is the diffusion constant and R is the effective interaction or annihilation radius of singlet excitons which is the separation at which the annihilation occurs. The Förster radius for exciton-exciton annihilation of 4.8 nm was adopted from previous research, which then gives a 3D diffusion coefficient[4].

Supplementary Figures

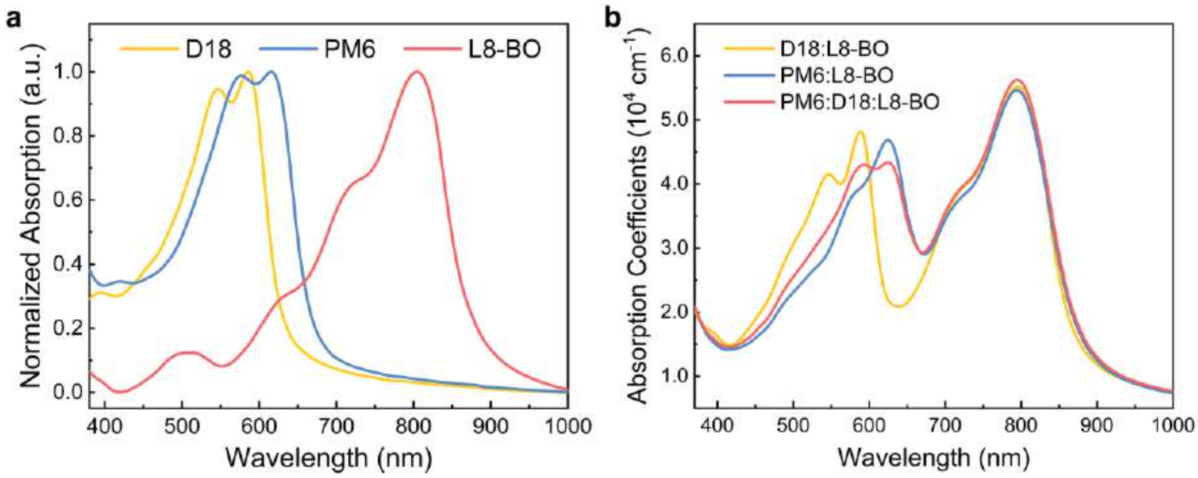

Supplementary Figure 1. UV–vis absorption spectra of D18, PM6, and L8-BO neat films (a) and D18:L8-BO, PM6:L8-BO, and PM6:D18:L8-BO blend films (b) processed by CF.

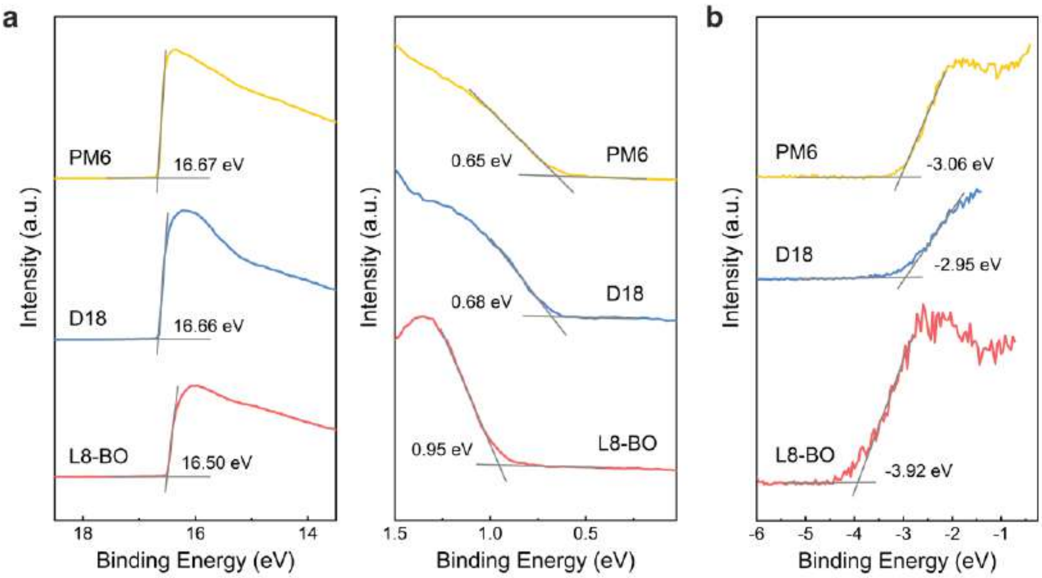

Supplementary Figure 2. UPS (a) and IPES (b) results of PM6, D18, and L8-BO. Fermi energy was determined by linear extrapolating the high binding energy portion of the spectrum, and HOMO energy level was referred to low binding energy onset. The LUMO energy level was obtained by linear extrapolation of the initial peak of IPES.

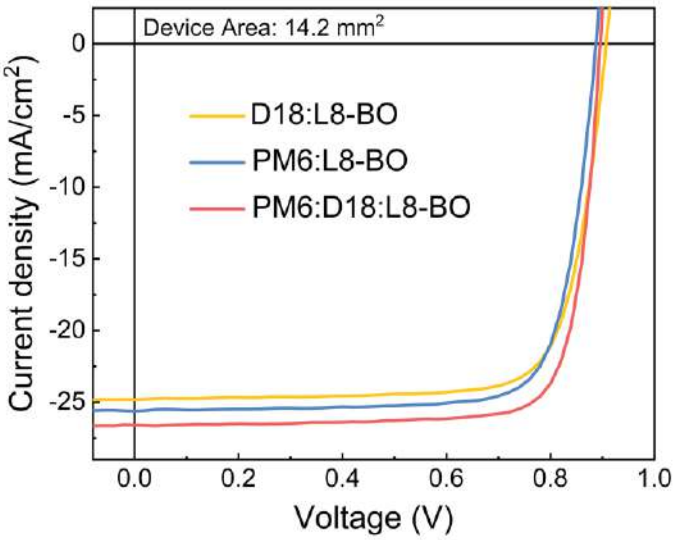

Supplementary Figure 3. *J–V* curves of the device based on D18:L8-BO, PM6:L8-BO, and PM6:D18:L8-BO (0.8:0.2:1.2) with a device area of 14.2 mm^2.

福建省计量科学研究院
国家光伏产业计量测试中心
FUJIAN METROLOGY INSTITUTE
NATIONAL PV INDUSTRY MEASUREMENT AND TESTING CENTER

171320110020

中国认可
国际互认
检测
TESTING
CNAS L01

检测报告

TESTING REPORT

报告编号：(MLY)Q3/20-000085
Report No.

委托者 Client：上海交通大学（SHANGHAI JIAO TONG UNIVERSITY）

委托者地址 Client address：上海市闵行区东川路 800 号（No. 800 Dongchuan Road, Minhang District, Shanghai ）

样品名称 Name of sample：有机太阳能电池（Organic Solar Cell）

制造厂 Manufactory：上海交通大学（SHANGHAI JIAO TONG UNIVERSITY）

型号规格 Type or Size：非富勒烯聚合物太阳能电池（Non-fullerene polymer solar cell）

样品编号 Number of sample：L12-M4

接收日期 Date of Receipt：2020-08-28

批准人 Approved by：罗海燕　　批准日期 Date of Approved：2020-09-03

核验员 Checked by：蔡健生　　核验日期 Date of Checked：2020-09-03

检测员 Tested by：陈彩云　　检测日期 Date of Tested：2020-08-28

地 址：福州市屏东路 9-3 号　电 话：0591－87842087　传 真：0591－87811744　邮 编：350003　监督电话：0591－87843005
Address: 9-3 Pingdong Road Fuzhou　Tel. 0591－87842087　Fax. 0591－87811744　Post Code. 350003　Tel.for Supervisor: 0591－87843005

未经本院批准，部分采用本证书内容无效。
Partly using this certificate will not be admitted unless allowed by fujian metrology institute

第 1 页/共 7 页
Page 1 of 7 Pages

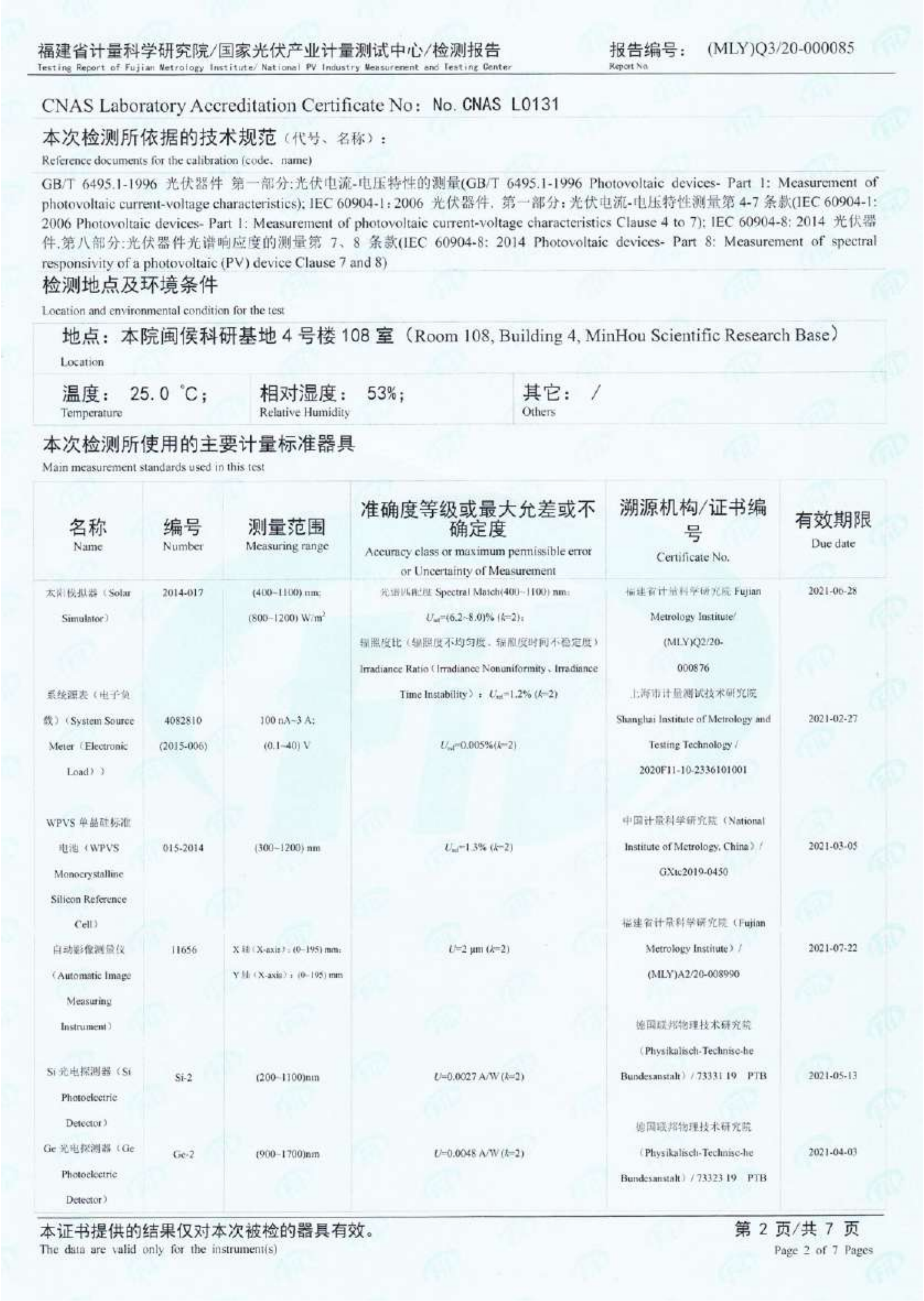

CNAS Laboratory Accreditation Certificate No： No. CNAS L0131

本次检测所依据的技术规范（代号、名称）：
Reference documents for the calibration (code、name)

GB/T 6495.1-1996 光伏器件 第一部分:光伏电流-电压特性的测量(GB/T 6495.1-1996 Photovoltaic devices- Part 1: Measurement of photovoltaic current-voltage characteristics); IEC 60904-1：2006 光伏器件，第一部分：光伏电流-电压特性测量第 4-7 条款(IEC 60904-1: 2006 Photovoltaic devices- Part 1: Measurement of photovoltaic current-voltage characteristics Clause 4 to 7); IEC 60904-8: 2014 光伏器件,第八部分:光伏器件光谱响应度的测量第 7、8 条款(IEC 60904-8: 2014 Photovoltaic devices- Part 8: Measurement of spectral responsivity of a photovoltaic (PV) device Clause 7 and 8)

检测地点及环境条件
Location and environmental condition for the test

地点：本院闽侯科研基地 4 号楼 108 室（Room 108, Building 4, MinHou Scientific Research Base）
Location

温度： 25.0 ℃； Temperature	相对湿度： 53%； Relative Humidity	其它： / Others

本次检测所使用的主要计量标准器具
Main measurement standards used in this test

名称 Name	编号 Number	测量范围 Measuring range	准确度等级或最大允差或不确定度 Accuracy class or maximum permissible error or Uncertainty of Measurement	溯源机构/证书编号 Certificate No.	有效期限 Due date
太阳模拟器（Solar Simulator）	2014-017	(400~1100) nm; (800~1200) W/m^2	光谱匹配度 Spectral Match(400~1100) nm：U_{rel}=(6.2~8.0)% (k=2)； 辐照度比（辐照度不均匀度、辐照度时间不稳定度）Irradiance Ratio（Irradiance Nonuniformity、Irradiance Time Instability）：U_{rel}=1.2% (k=2)	福建省计量科学研究院 Fujian Metrology Institute/ (MLY)Q2/20-000876	2021-06-28
系统源表（电子负载）（System Source Meter（Electronic Load））	4082810 (2015-006)	100 nA~3 A; (0.1~40) V	U_{rel}=0.005%(k=2)	上海市计量测试技术研究院 Shanghai Institute of Metrology and Testing Technology / 2020F11-10-2336101001	2021-02-27
WPVS 单晶硅标准电池（WPVS Monocrystalline Silicon Reference Cell）	015-2014	(300~1200) nm	U_{rel}=1.3% (k=2)	中国计量科学研究院（National Institute of Metrology, China）/ GXtc2019-0450	2021-03-05
自动影像测量仪（Automatic Image Measuring Instrument）	11656	X 轴（X-axis）：(0~195) mm; Y 轴（X-axis）：(0~195) mm	U=2 μm (k=2)	福建省计量科学研究院（Fujian Metrology Institute）/ (MLY)A2/20-008990	2021-07-22
Si 光电探测器（Si Photoelectric Detector）	Si-2	(200~1100)nm	U=0.0027 A/W (k=2)	德国联邦物理技术研究院（Physikalisch-Technisc-he Bundesanstalt）/ 73331 19 PTB	2021-05-13
Ge 光电探测器（Ge Photoelectric Detector）	Ge-2	(900~1700)nm	U=0.0048 A/W (k=2)	德国联邦物理技术研究院（Physikalisch-Technisc-he Bundesanstalt）/ 73323 19 PTB	2021-04-03

本证书提供的结果仅对本次被检的器具有效。
The data are valid only for the instrument(s)

检测数据/结果：
Data/Results of Test

1 标准测试条件 STC Standard Test Condition (STC)：

总辐照度 Total Irradiance：1000 W/m^2
被测电池温度 Temperature：25.0 ℃
光谱分布 Spectral Distribution：AM1.5G

2. STC 条件下测量数据
Measurement Data under STC

测试次数 Test Times	I_{sc} (mA)	V_{oc} (V)	I_{MPP} (mA)	V_{MPP} (V)	P_{MPP} (mW)	FF (%)	η (%)
1	0.8181	0.8925	0.7765	0.7628	0.5923	81.12	19.21
2	0.8234	0.8912	0.7768	0.7637	0.5932	80.84	19.23
3	0.8269	0.8904	0.7596	0.7740	0.5879	79.85	19.06
平均值 Average Value	0.8228	0.8914	0.7710	0.7668	0.5911	80.60	19.17

失配因子 Mismatch factor: 0.9900

3. STC 下电流-电压特性曲线和功率-电压特性曲线
I-V & P-V Characteristic Curves under STC

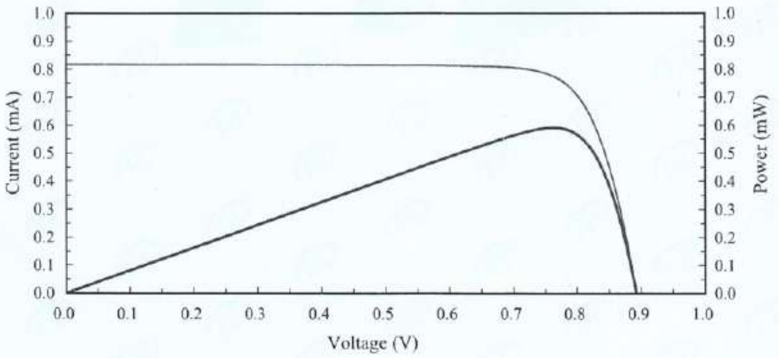

图 1 STC 下电流-电压特性曲线和功率-电压特性曲线

Figure 1. I-V and P-V characteristic curves of the measured sample under STC

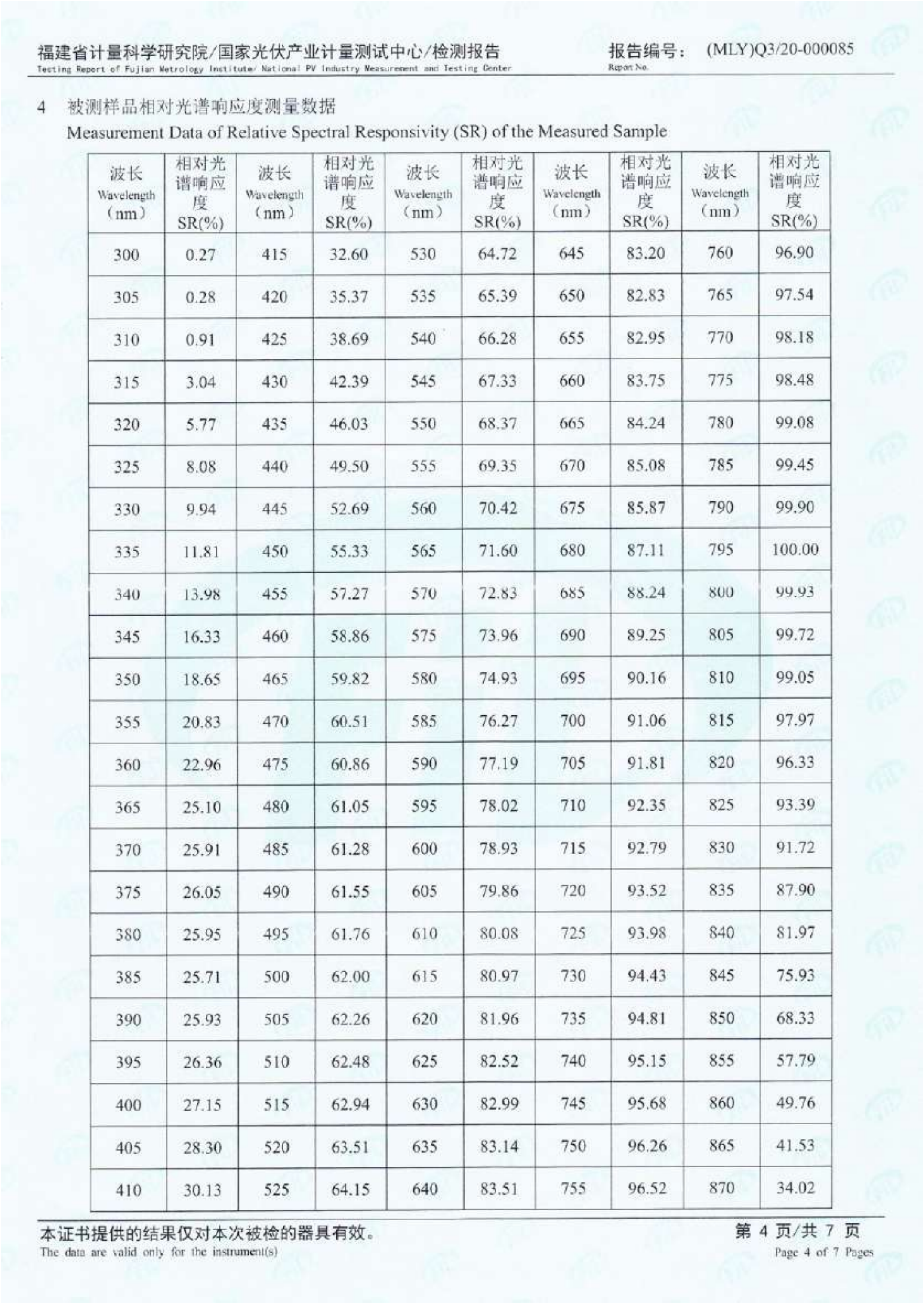

4 被测样品相对光谱响应度测量数据

Measurement Data of Relative Spectral Responsivity (SR) of the Measured Sample

波长 Wavelength (nm)	相对光谱响应度 SR(%)	波长 Wavelength (nm)	相对光谱响应度 SR(%)	波长 Wavelength (nm)	相对光谱响应度 SR(%)	波长 Wavelength (nm)	相对光谱响应度 SR(%)	波长 Wavelength (nm)	相对光谱响应度 SR(%)
300	0.27	415	32.60	530	64.72	645	83.20	760	96.90
305	0.28	420	35.37	535	65.39	650	82.83	765	97.54
310	0.91	425	38.69	540	66.28	655	82.95	770	98.18
315	3.04	430	42.39	545	67.33	660	83.75	775	98.48
320	5.77	435	46.03	550	68.37	665	84.24	780	99.08
325	8.08	440	49.50	555	69.35	670	85.08	785	99.45
330	9.94	445	52.69	560	70.42	675	85.87	790	99.90
335	11.81	450	55.33	565	71.60	680	87.11	795	100.00
340	13.98	455	57.27	570	72.83	685	88.24	800	99.93
345	16.33	460	58.86	575	73.96	690	89.25	805	99.72
350	18.65	465	59.82	580	74.93	695	90.16	810	99.05
355	20.83	470	60.51	585	76.27	700	91.06	815	97.97
360	22.96	475	60.86	590	77.19	705	91.81	820	96.33
365	25.10	480	61.05	595	78.02	710	92.35	825	93.39
370	25.91	485	61.28	600	78.93	715	92.79	830	91.72
375	26.05	490	61.55	605	79.86	720	93.52	835	87.90
380	25.95	495	61.76	610	80.08	725	93.98	840	81.97
385	25.71	500	62.00	615	80.97	730	94.43	845	75.93
390	25.93	505	62.26	620	81.96	735	94.81	850	68.33
395	26.36	510	62.48	625	82.52	740	95.15	855	57.79
400	27.15	515	62.94	630	82.99	745	95.68	860	49.76
405	28.30	520	63.51	635	83.14	750	96.26	865	41.53
410	30.13	525	64.15	640	83.51	755	96.52	870	34.02

4 被测样品相对光谱响应度测量数据（续）
Measurement Data of Relative Spectral Responsivity (SR) of the Measured Sample (continued)

波长 Wavelength（nm）	相对光谱响应度 SR(%)	波长 Wavelength（nm）	相对光谱响应度 SR(%)	波长 Wavelength（nm）	相对光谱响应度 SR(%)	波长 Wavelength（nm）	相对光谱响应度 SR(%)	波长 Wavelength（nm）	相对光谱响应度 SR(%)
875	27.42	895	10.80	915	3.64	935	1.24	/	/
880	21.14	900	8.02	920	2.51	940	0.88	/	/
885	16.32	905	6.22	925	2.12	945	0.67	/	/
890	14.52	910	4.68	930	1.60	950	0.55	/	/

5 相对光谱响应度曲线
Relative Spectral Responsivity Curve

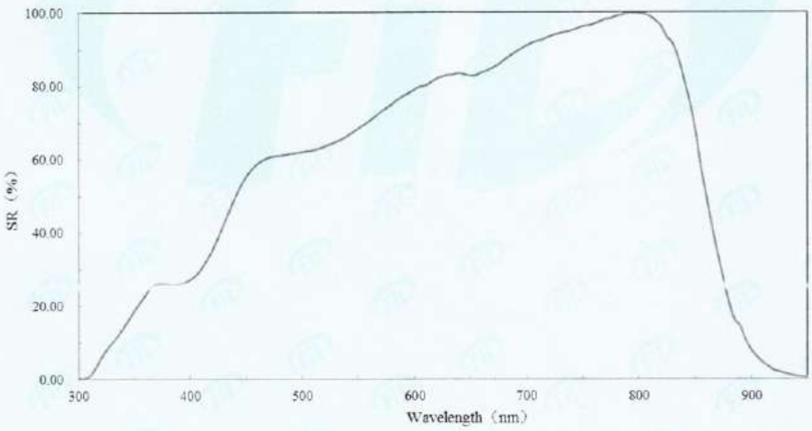

图 2 相对光谱响应度曲线
Figure 2. Relative spectral responsivity curve of the measured sample

6 样品信息

Pictures of the Measured Sample

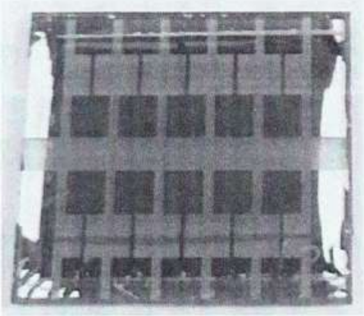

图 3 被测样品的正面图像

Figure 3. Obverse side of the measured sample

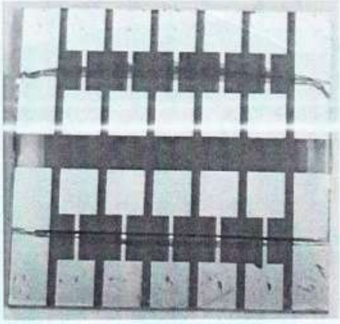

图 4 被测样品的反面图像

Figure 4. Reverse side of the measured sample

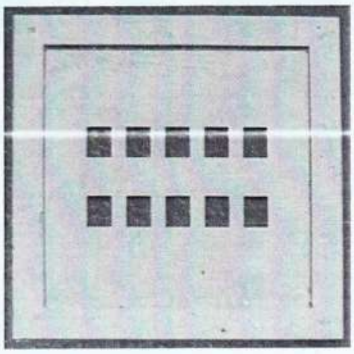

图 5 测试所用掩膜板

Figure 5. Mask used during test

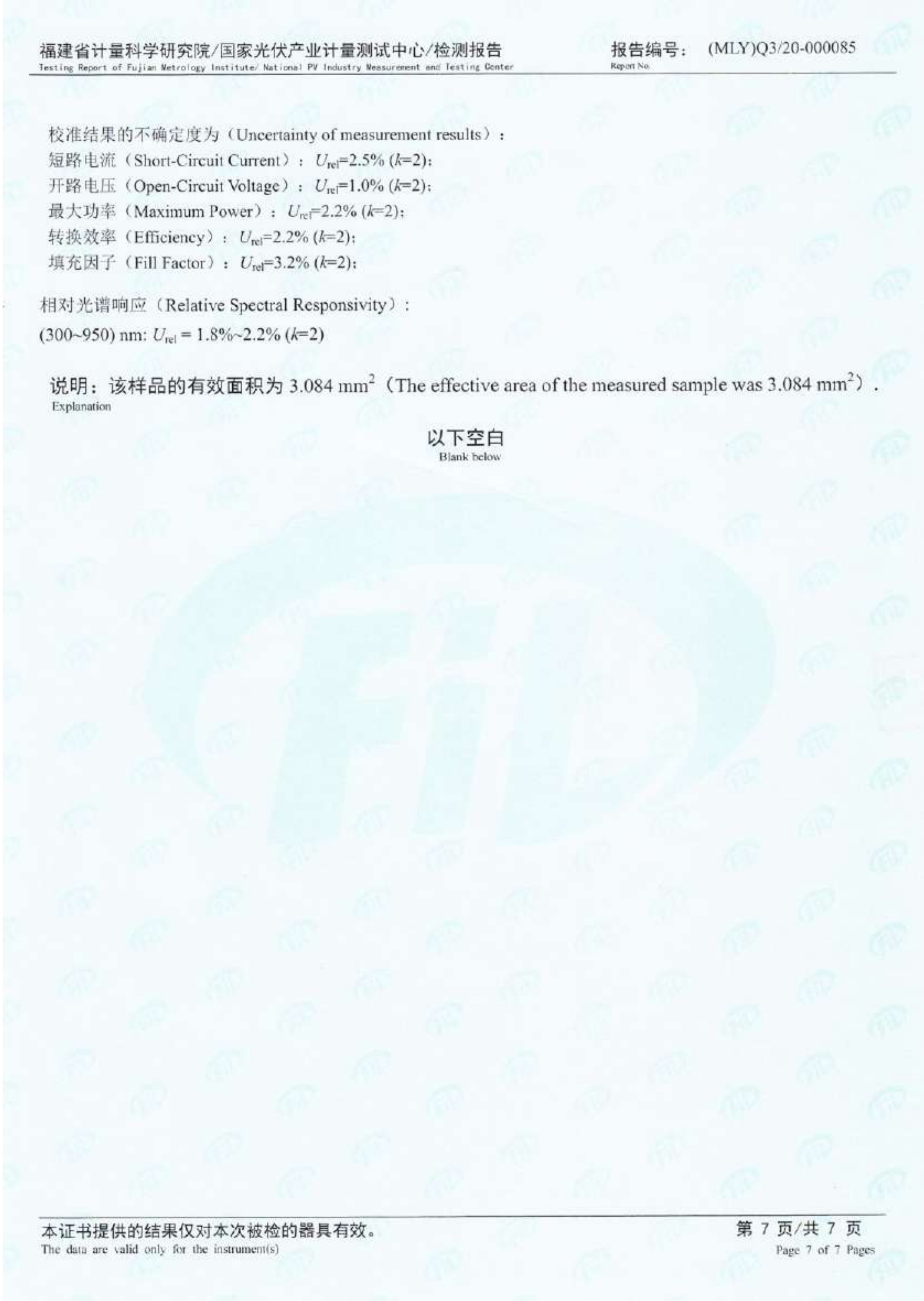

福建省计量科学研究院/国家光伏产业计量测试中心/检测报告
Testing Report of Fujian Metrology Institute/ National PV Industry Measurement and Testing Center

报告编号： (MLY)Q3/20-000085
Report No.

校准结果的不确定度为（Uncertainty of measurement results）：
短路电流（Short-Circuit Current）：U_{rel}=2.5% (k=2);
开路电压（Open-Circuit Voltage）：U_{rel}=1.0% (k=2);
最大功率（Maximum Power）：U_{rel}=2.2% (k=2);
转换效率（Efficiency）：U_{rel}=2.2% (k=2);
填充因子（Fill Factor）：U_{rel}=3.2% (k=2);

相对光谱响应（Relative Spectral Responsivity）：
(300~950) nm: U_{rel} = 1.8%~2.2% (k=2)

说明：该样品的有效面积为 3.084 mm^2（The effective area of the measured sample was 3.084 mm^2）.
Explanation

以下空白
Blank below

本证书提供的结果仅对本次被检的器具有效。
The data are valid only for the instrument(s)

第 7 页/共 7 页
Page 7 of 7 Pages

Supplementary Figure 4. Original images of the OSC certificate results by the National Photovoltaic Industry Metrology and Testing Center (NPVM, China). The device is measured with a mask of 3.084 mm^2 and gives a PCE of 19.17%.

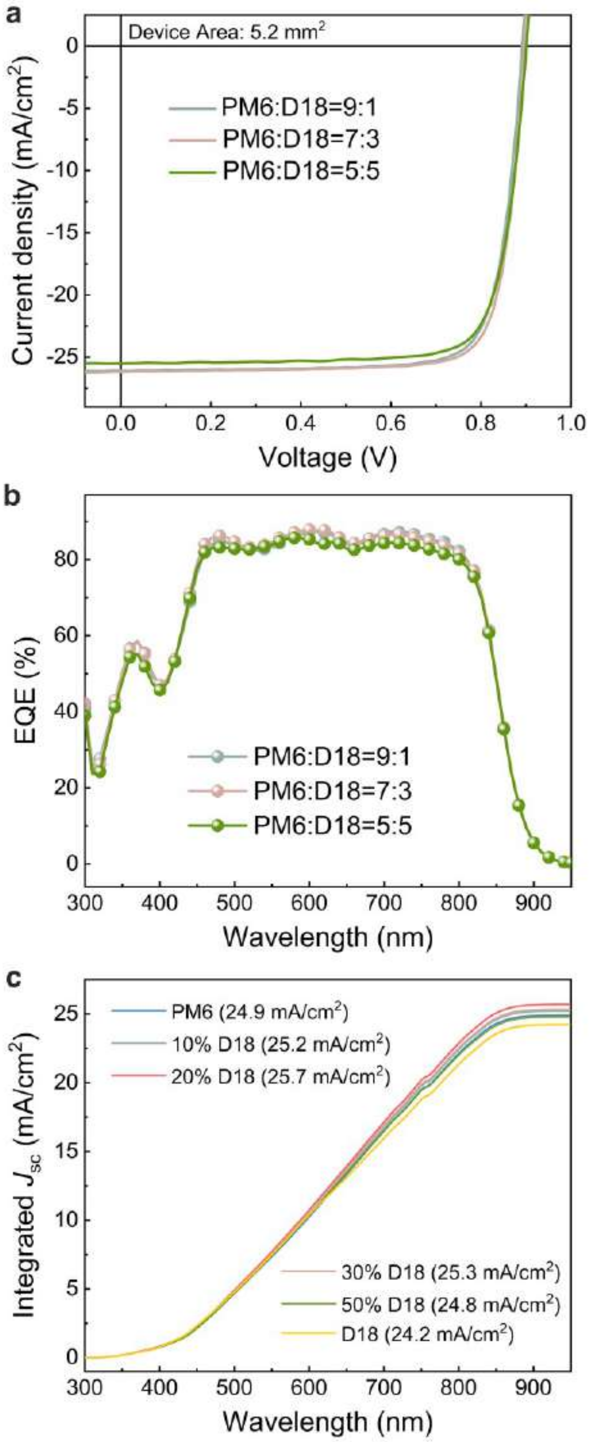

Supplementary Figure 5. *J*–*V* (a) and EQE (b) curves of the device based on PM6:D18:L8-BO under different PM6:D18 ratios. (c) The integrated J_{sc} curves under different donor conditions (device area was 5.2 mm^2).

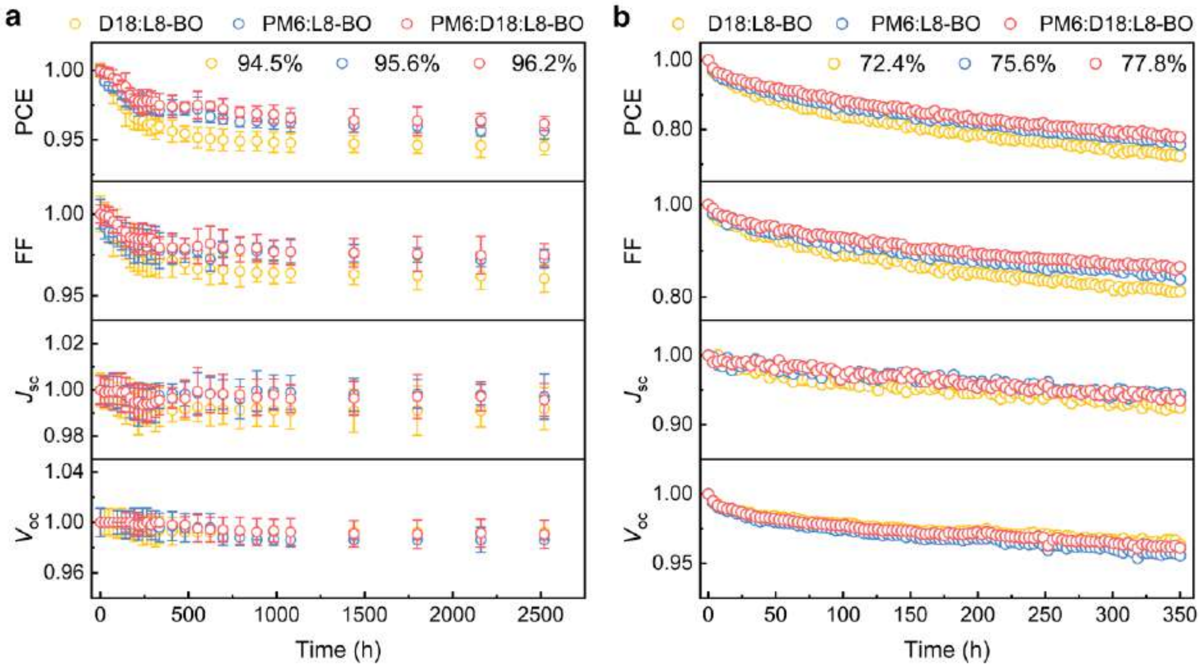

Supplementary Figure 6. Storage (a) and illumination (b) stability of the device based on D18:L8-BO, PM6:L8-BO, and PM6:D18:L8-BO. The storage stability was tested for 2520 hours, the device was encapsulated and stored in a glove box at 25 ℃. The illumination stability was tested for 350 hours. The device was encapsulated and then tested in the atmosphere under the illumination of AM 1.5 G, 100 mW/cm^2.

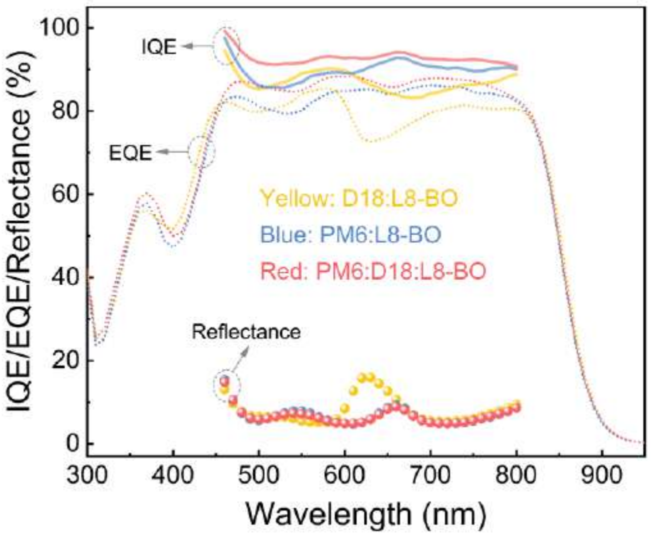

Supplementary Figure 7. IQE, EQE, and reflectance curves of binary and ternary devices.

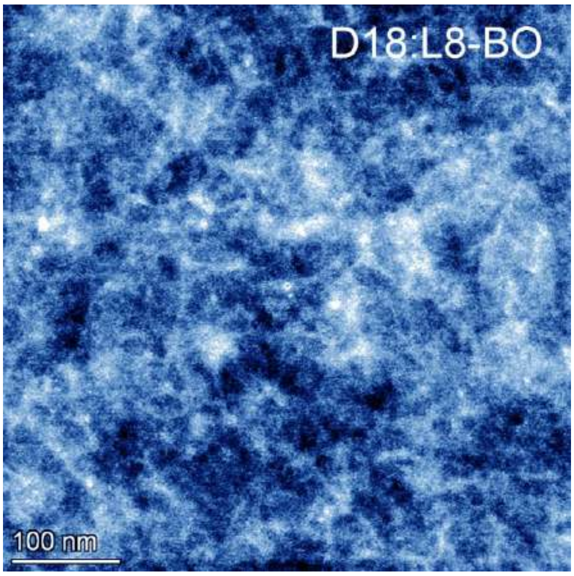

Supplementary Figure 8. TEM image of D18:L8-BO blended film.

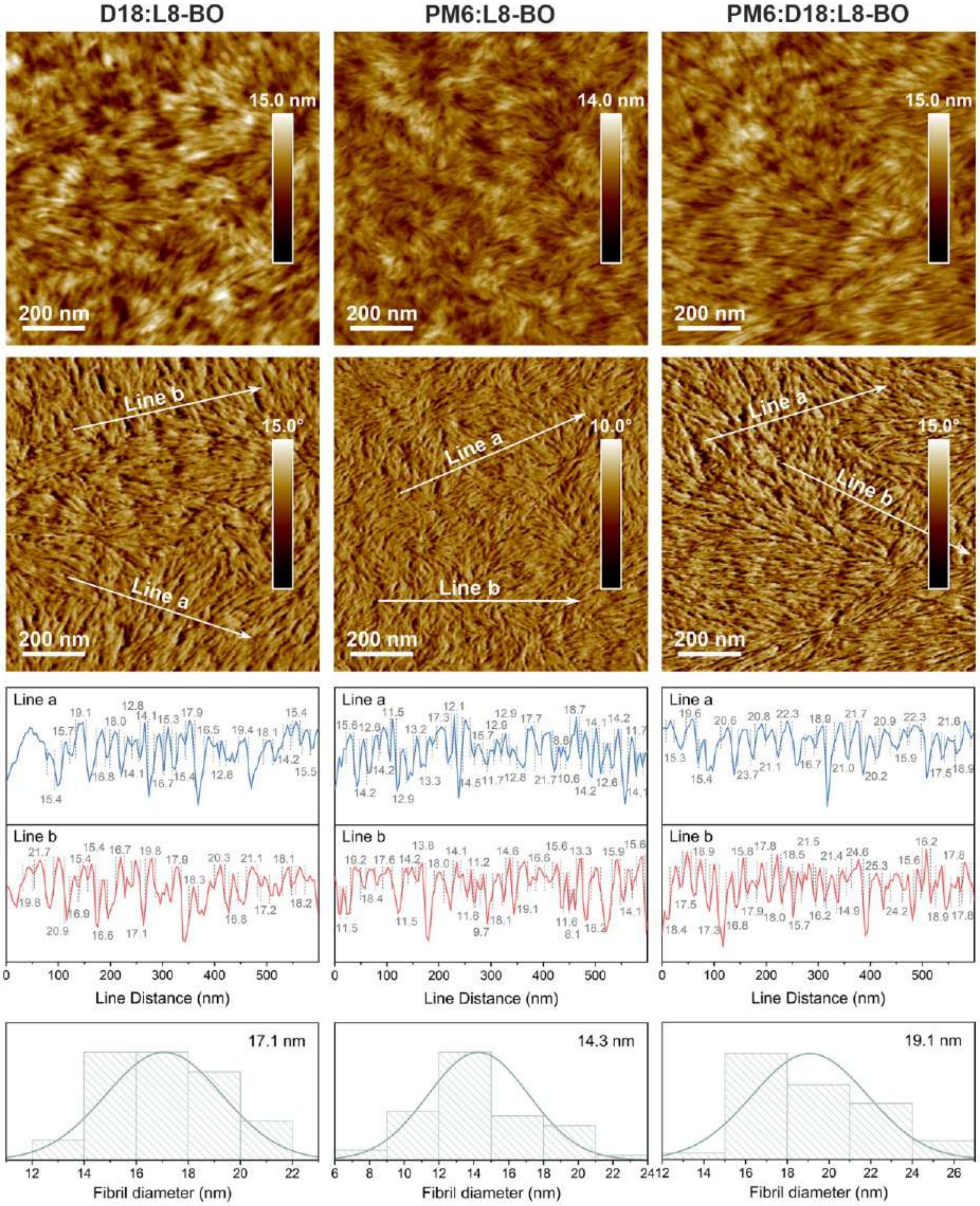

Supplementary Figure 9. AFM height (first row) and phase (second row) images of D18:L8-BO, PM6:L8-BO, and PM6:D18:L8-BO (0.8:0.2:1.2) blended films. The line profile to obtain the fibril width (third row) and the statistical distribution (fourth row) for the three blended films.

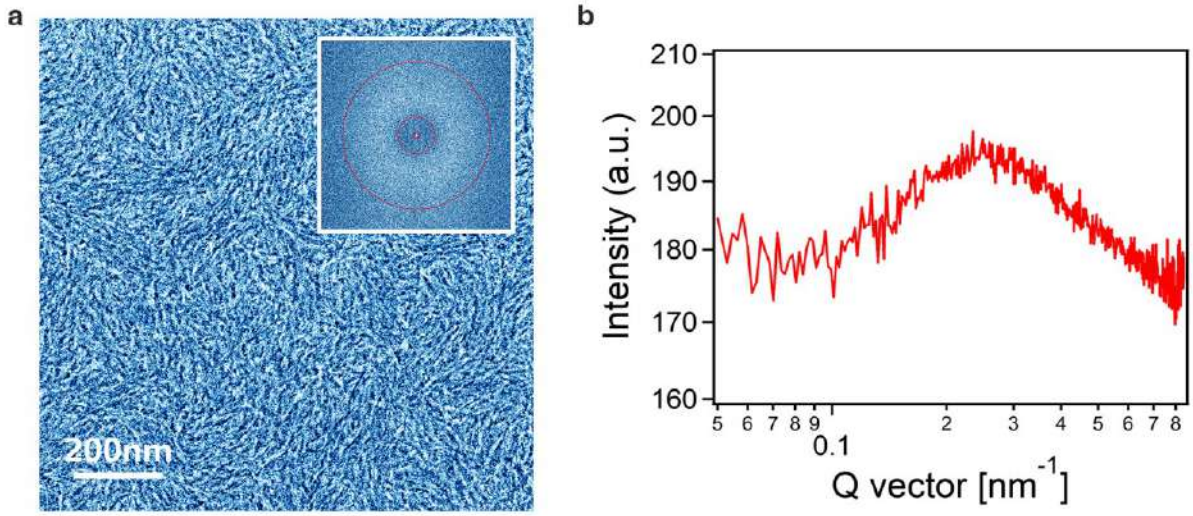

Supplementary Figure 10. (a) SEM image of PM6:D18:L8-BO=0.8:0.2:1.2 blended film (insert is Fourier transformed image). (b) Circle integration of the 2D Fourier transformed image.

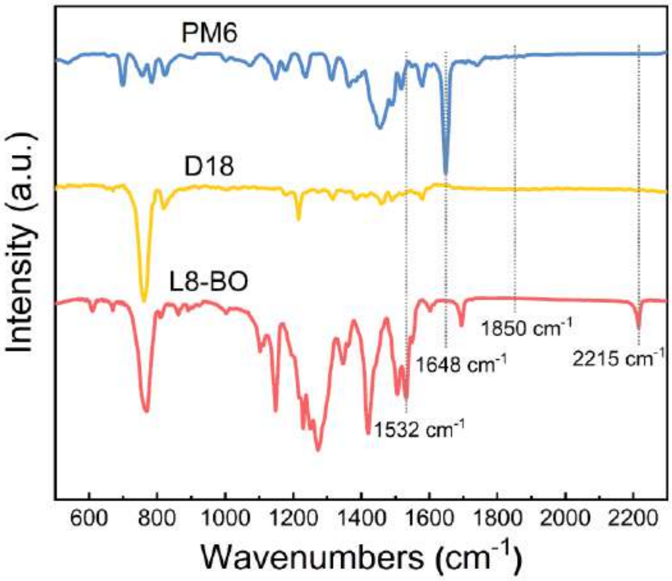

Supplementary Figure 11. FTIR spectra of PM6, D18, and L8-BO.

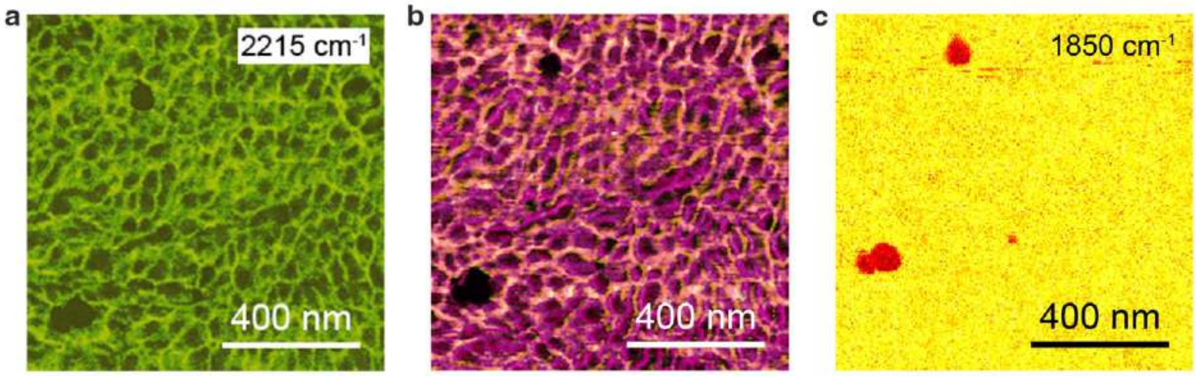

Supplementary Figure 12. (a) PiFM image at the wavenumber of 2215 cm^{-1} (at this wavenumber, L8-BO was absorbed, which was consistent with the PiFM image at 1532 cm^{-1}. Further confirmed the fibril network structure formed by L8-BO). (b) The PiFM images overlapped at the wavenumber of 1532 cm^{-1} and 1648 cm^{-1} (The black spots in the image are used for positioning). (c) PiFM image at the wavenumber of 1850 cm^{-1} (at this wavenumber, both PM6, D18, and L8-BO have no signal).

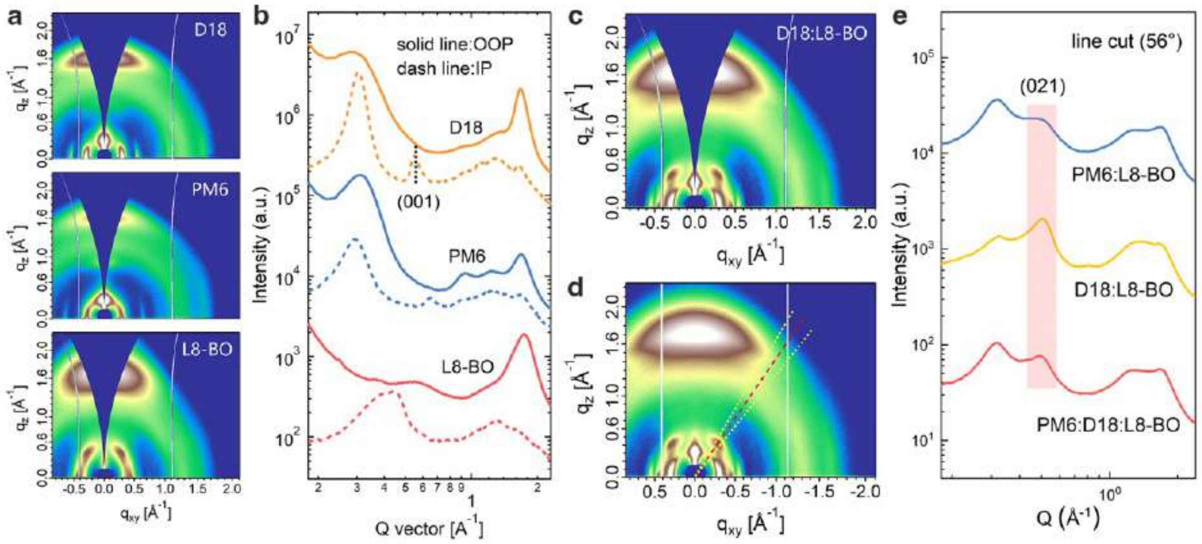

Supplementary Figure 13. (a) 2D GIXD patterns of neat D18, PM6, and L8-BO films. (b) The in-plane and out-of-plane line cut profiles of the 2D GIXD data based on neat films. (c) 2D GIXD patterns of D18:L8-BO blended film. (d) The line cut profiles diagram of (021) diffraction peak. (e) The line cut profiles of the 2D GIXD data based on binary and ternary blend films in a 56° azimuthal angle plane.

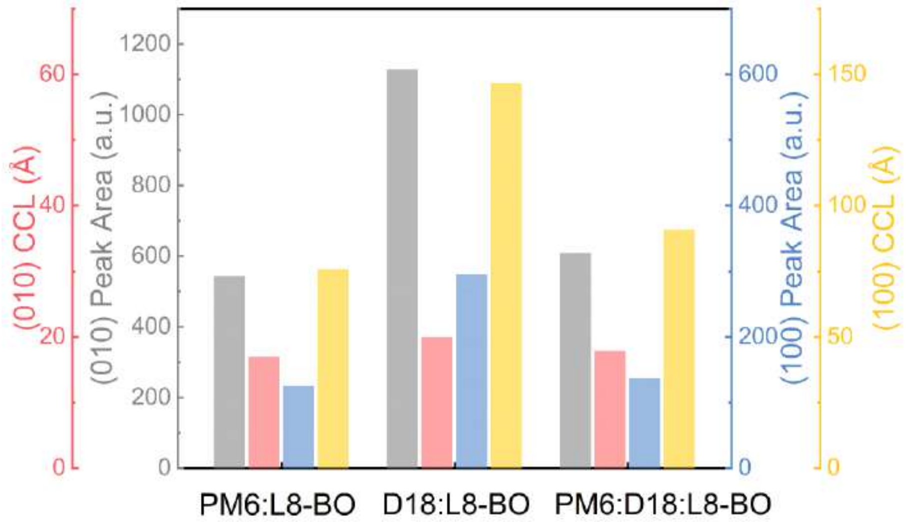

Supplementary Figure 14. Peak area and CCL of (010) and (100) diffraction peaks for D18:L8-BO, PM6:L8-BO, and PM6:D18:L8-BO (0.8:0.2:1.2) blended films.

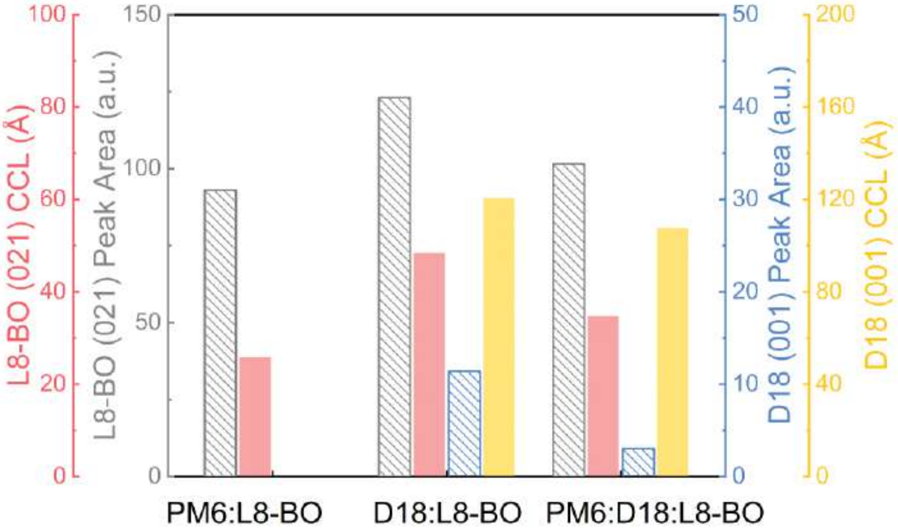

Supplementary Figure 15. Peak area and CCL of L8-BO (021) and D18 (001) diffraction peaks for D18:L8-BO, PM6:L8-BO, and PM6:D18:L8-BO (0.8:0.2:1.2) blended films.

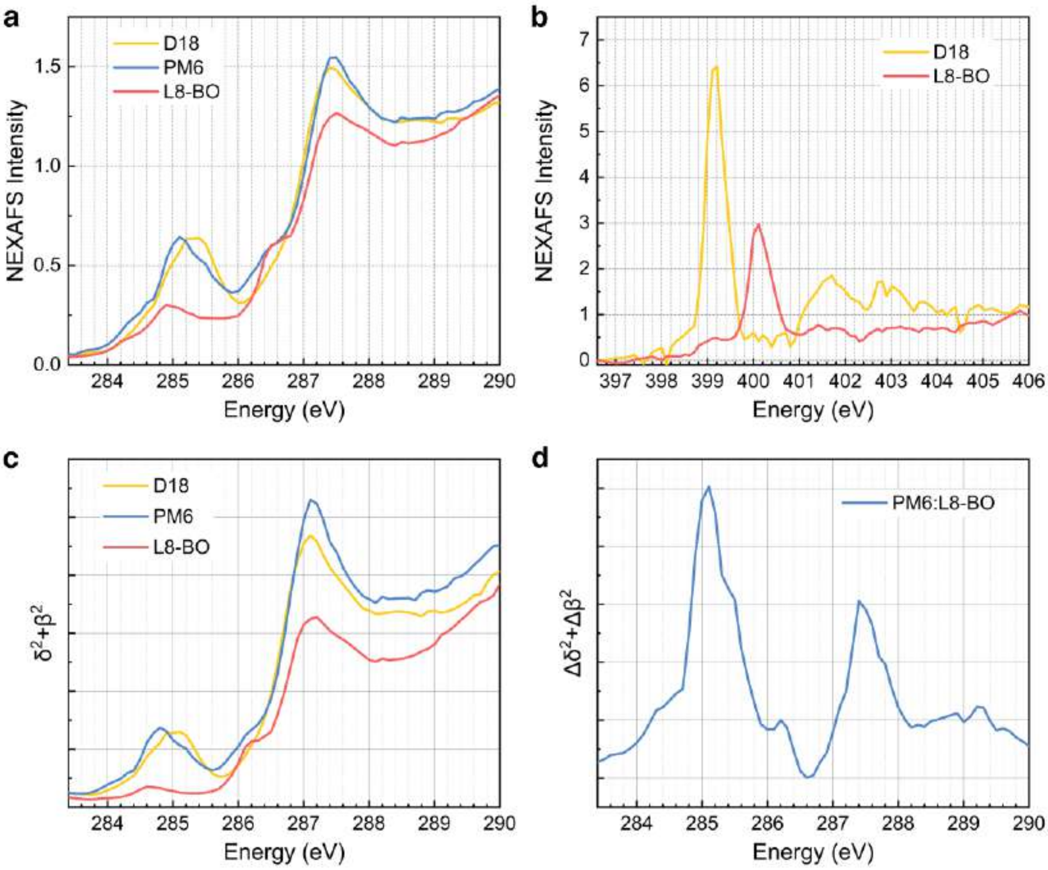

Supplementary Figure 16. (a,b) The near-edge x-ray absorption fine structure spectroscopy (NEXAFS) of neat films under different energy ranges. Contrast functions for the neat (c) and blended (d) materials with vacuum (n=1). The mass density of each material was assumed to be 1.0 g/cm^3.

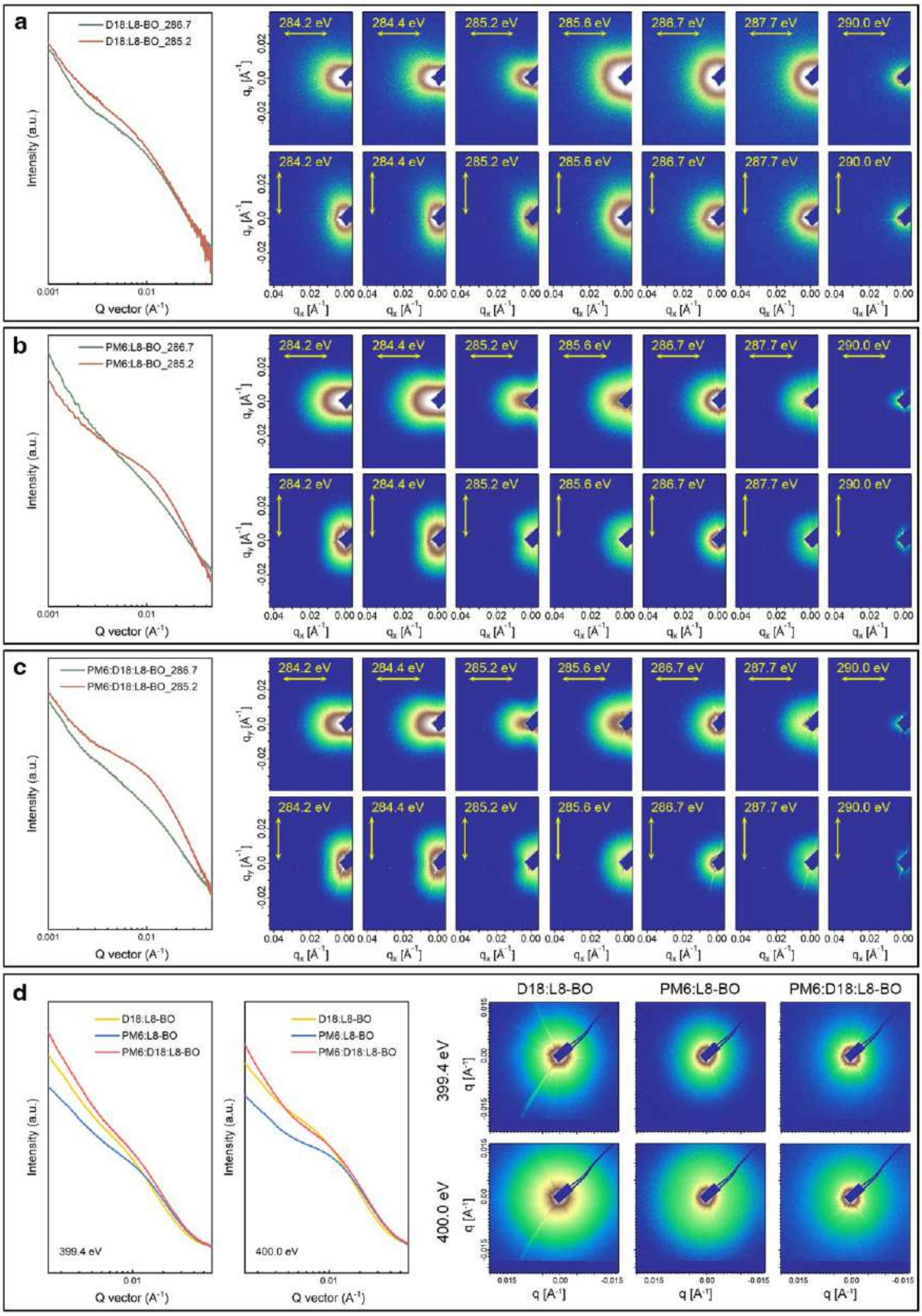

Supplementary Figure 17. CK-RSoXS profiles and polarized RSoXS of D18:L8-BO (a), PM6:L8-BO (b), and PM6:D18:L8-BO (c) blends under different photon energies. (d) NK-RSoXS profiles of D18:L8-BO, PM6:L8-BO, and PM6:D18:L8-BO blends under different photon energies.

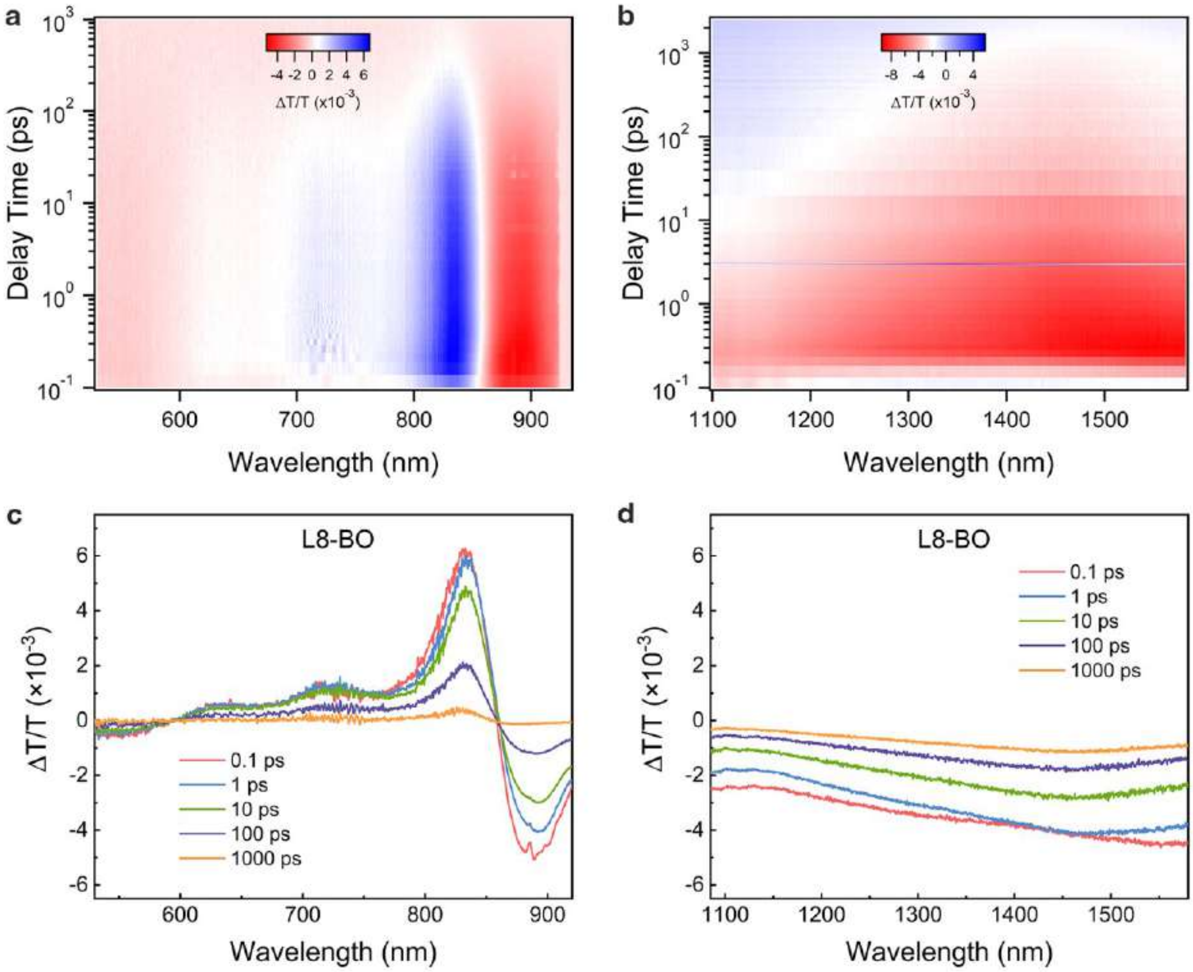

Supplementary Figure 18. The color plot of fs transient absorption spectra of neat L8-BO film under 750 nm (a,b) excitation and the representative fs transient absorption spectra of neat L8-BO film at indicated delay times under 750 nm (c,d) excitation.

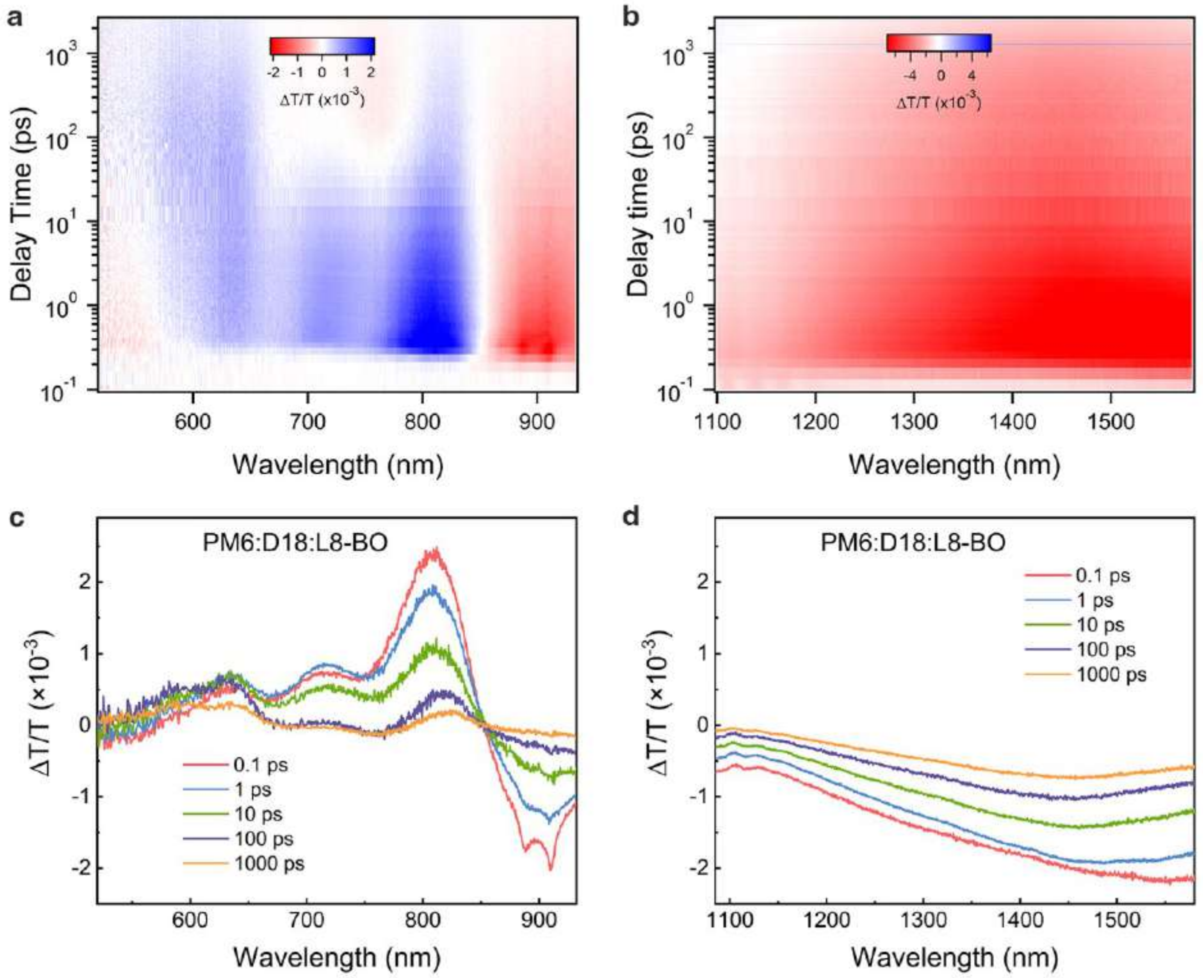

Supplementary Figure 19. The color plot of fs transient absorption spectra of PM6:D18:L8-BO (0.8:0.2:1.2) film under 750 nm (a,b) excitation and the representative fs transient absorption spectra of PM6:D18:L8-BO (0.8:0.2:1.2) film at indicated delay times under 750 nm (c,d) excitation.

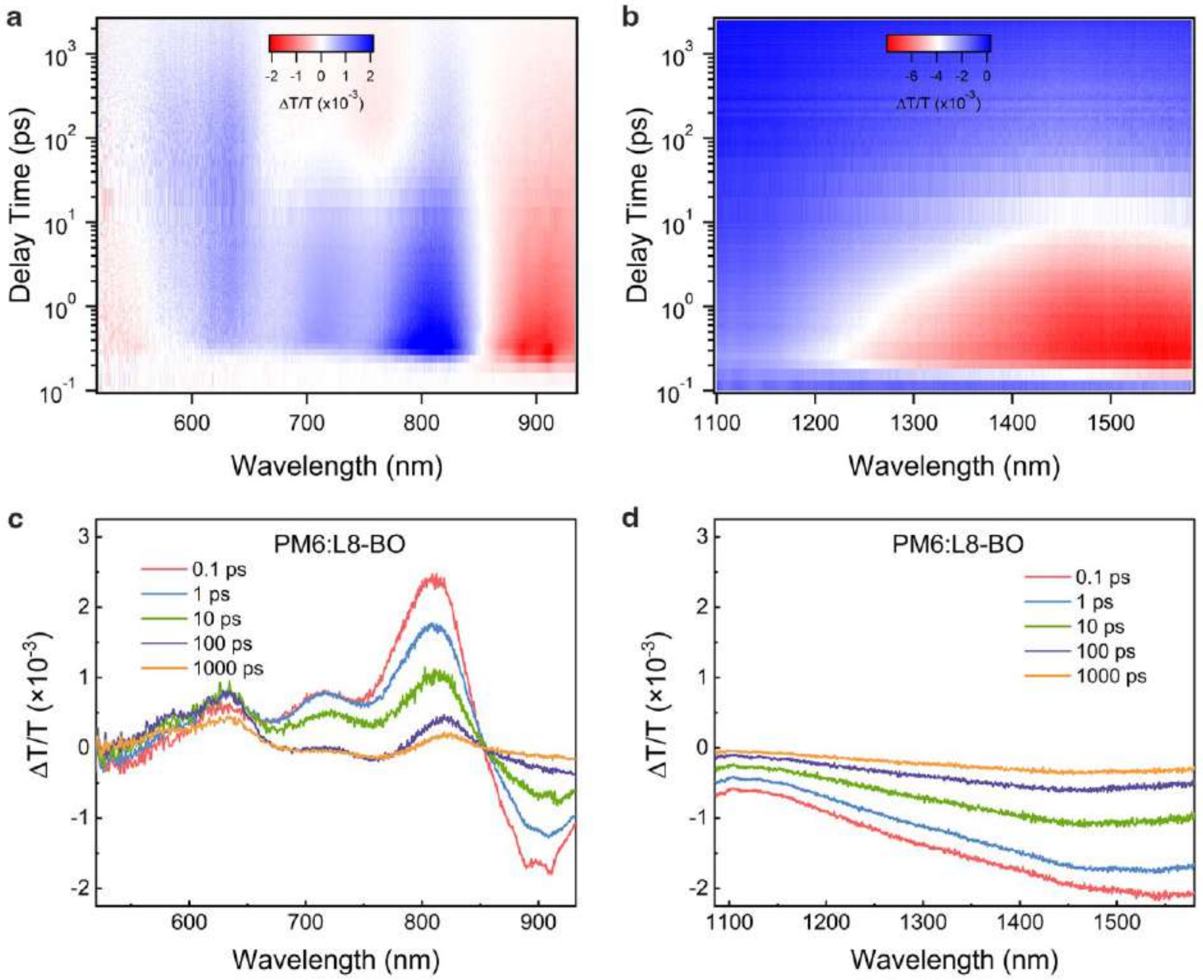

Supplementary Figure 20. The color plot of fs transient absorption spectra of PM6:L8-BO film under 750 nm (a,b) excitation and the representative fs transient absorption spectra of PM6:L8-BO film at indicated delay times under 750 nm (c,d) excitation.

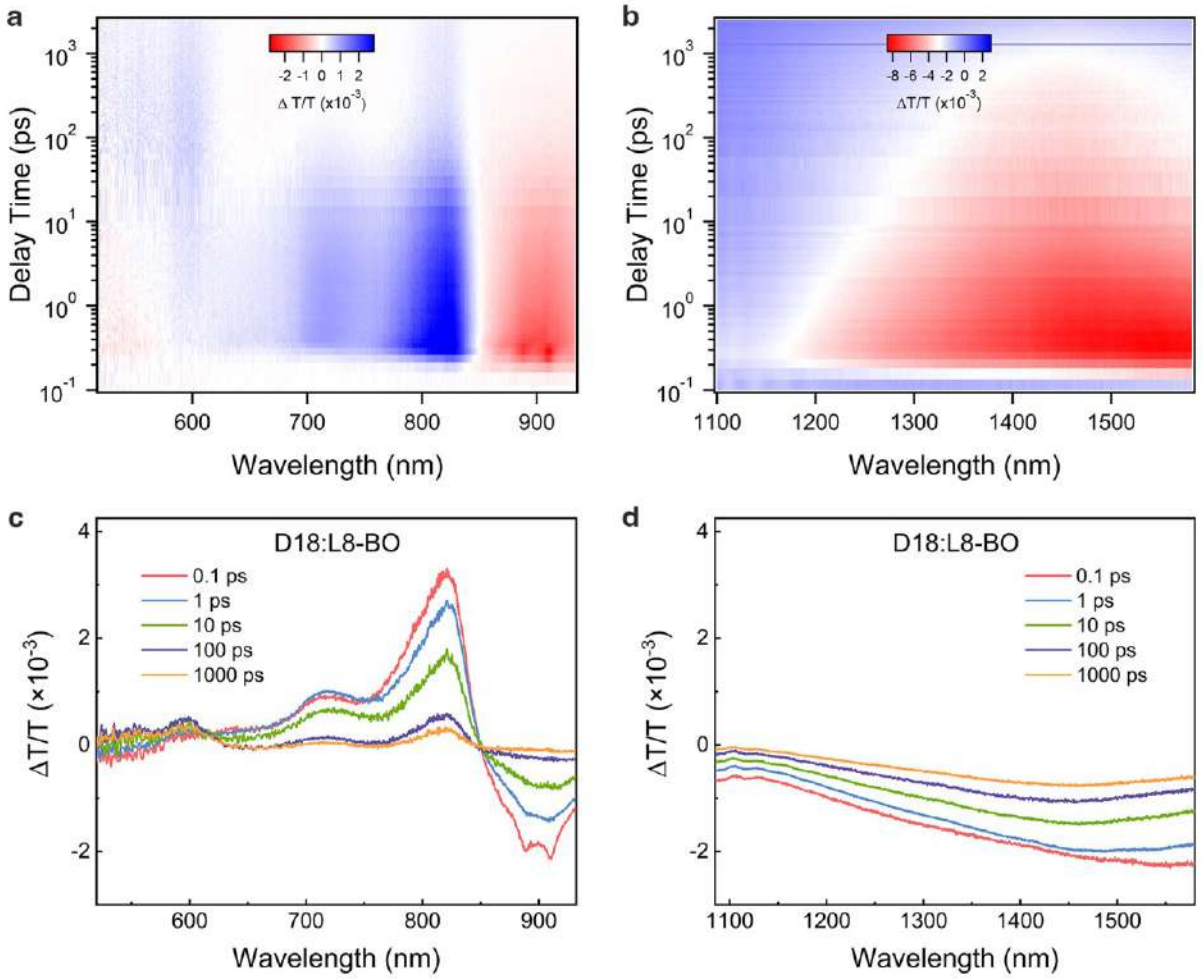

Supplementary Figure 21. The color plot of fs transient absorption spectra of D18:L8-BO film under 750 nm (a,b) excitation and the representative fs transient absorption spectra of D18:L8-BO film at indicated delay times under 750 nm (c,d) excitation.

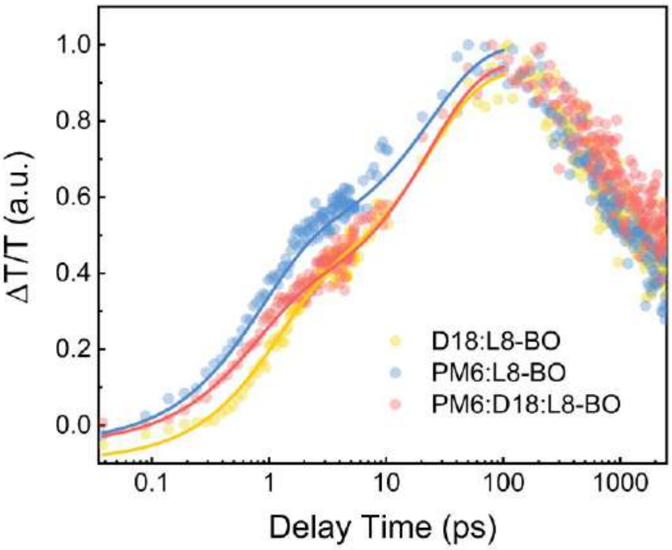

Supplementary Figure 22. The hole transfer process in D18:L8-BO (yellow dots), PM6:L8-BO (blue dots), and PM6:D18:L8-BO (red dots) blended films (the solid line is the fitting curves).

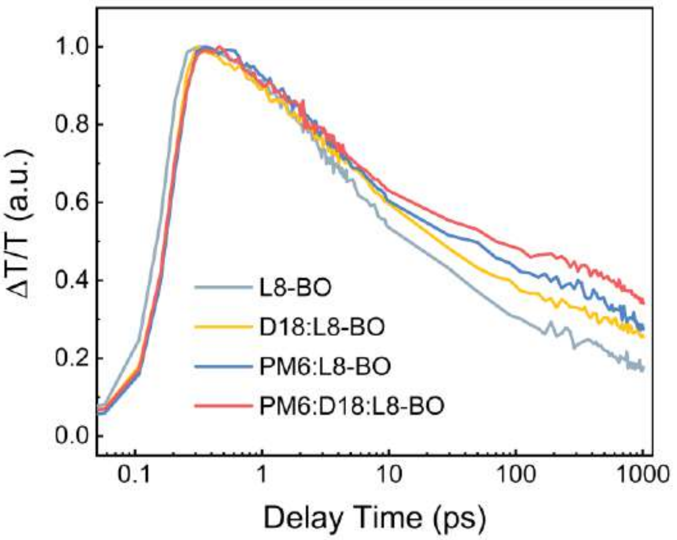

Supplementary Figure 23. The TA kinetics of polaron state of neat L8-BO and three blend films.

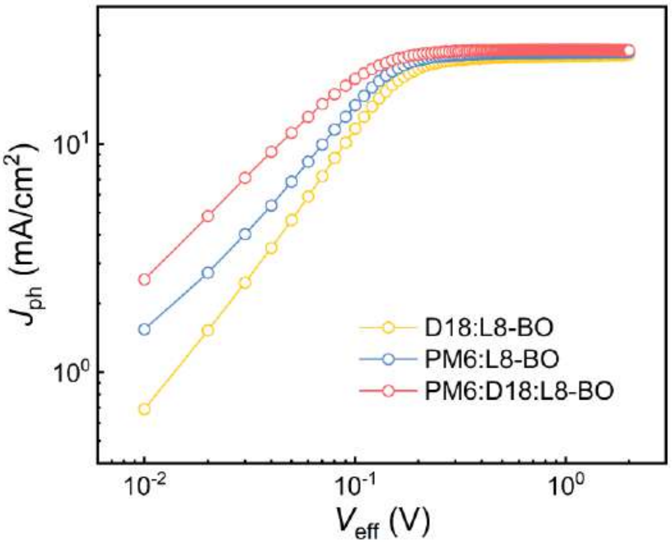

Supplementary Figure 24. Characteristics of the photocurrent density versus effective voltage ($J_{ph} \sim V_{eff}$) based on D18:L8-BO, PM6:L8-BO, and PM6:D18:L8-BO (0.8:0.2:1.2). $J_{ph} = J_L - J_D$, J_L and J_D are light and dark current density, $V_{eff} = V_0 - V_{appl}$, V_{appl} is the applied voltage and V_0 is the voltage when $J_{ph} = 0$ mA cm^{-2}.

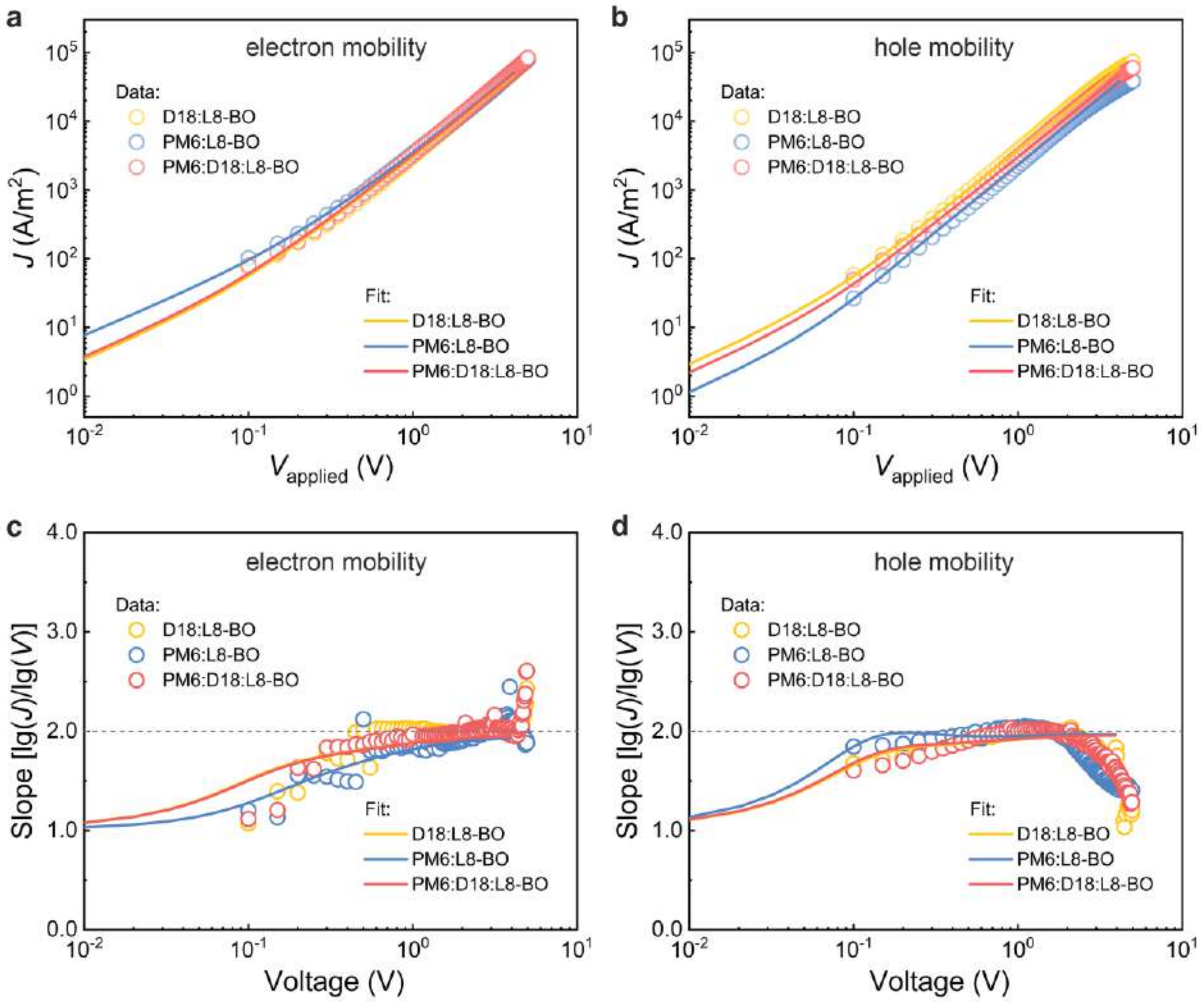

Supplementary Figure 25. Mobility measurements. SCLC measurement for electron-only (a) and hole-only (b) devices under different components. The slopes of each curve are shown in (c) and (d). In all devices, a maximum slope of ~2 is observed, indicating a negligible role of trap states. The fitting was done using a full drift diffusion model using gpvdm, and the details of fitting are presented in the methods section in Supplementary Information.

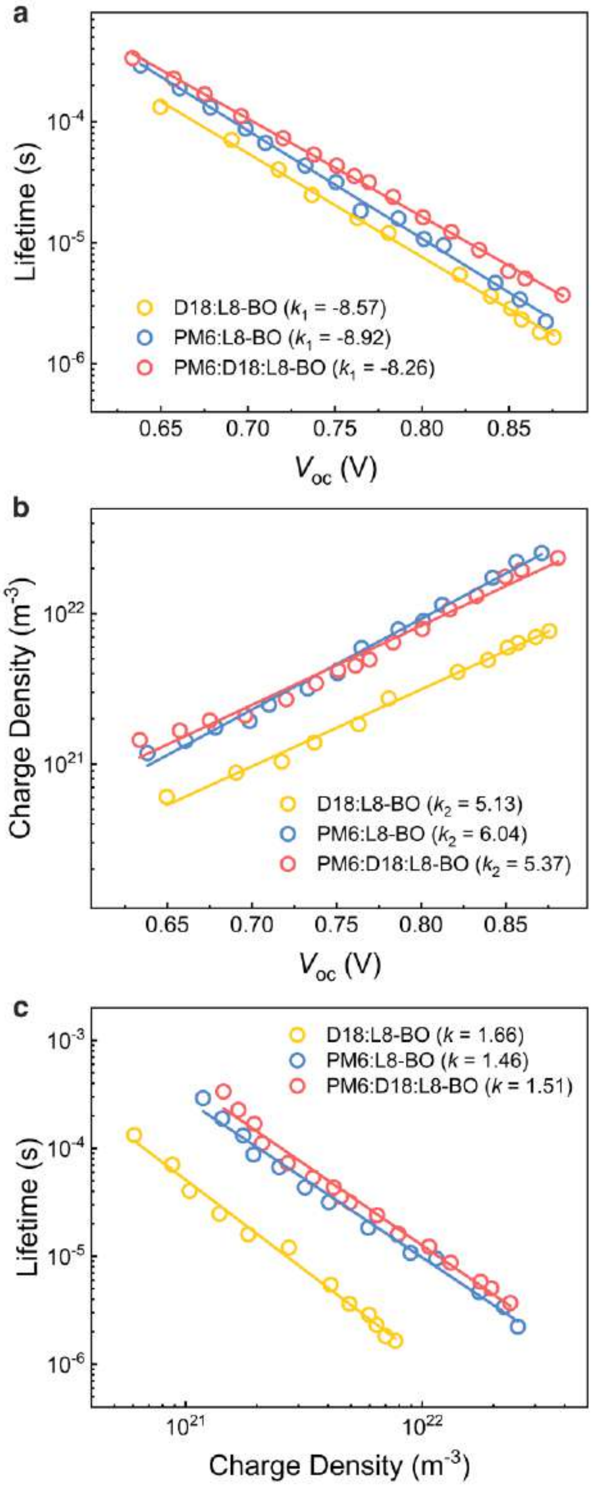

Supplementary Figure 26. Lifetime (a) and charge-carriers density (b) under different V_{oc} conditions. (c) Charge lifetime in the devices as a function of charge density. The solid lines represent the best fit to power-law dependence.

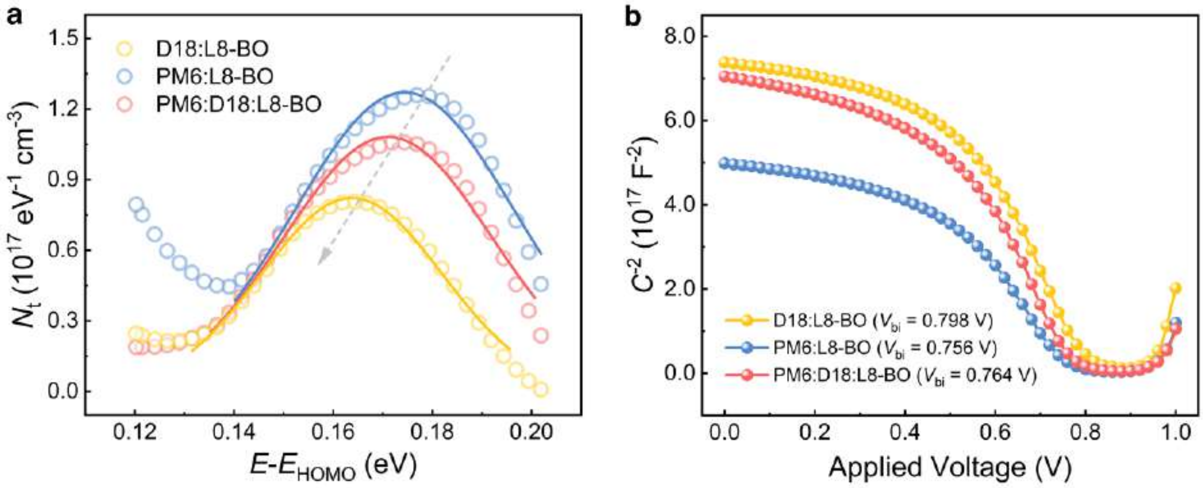

Supplementary Figure 27. The defects density of state (a) and built-in potential (b) of binary and ternary devices measured following the Mott-Schottky method at 10 kHz in the dark.

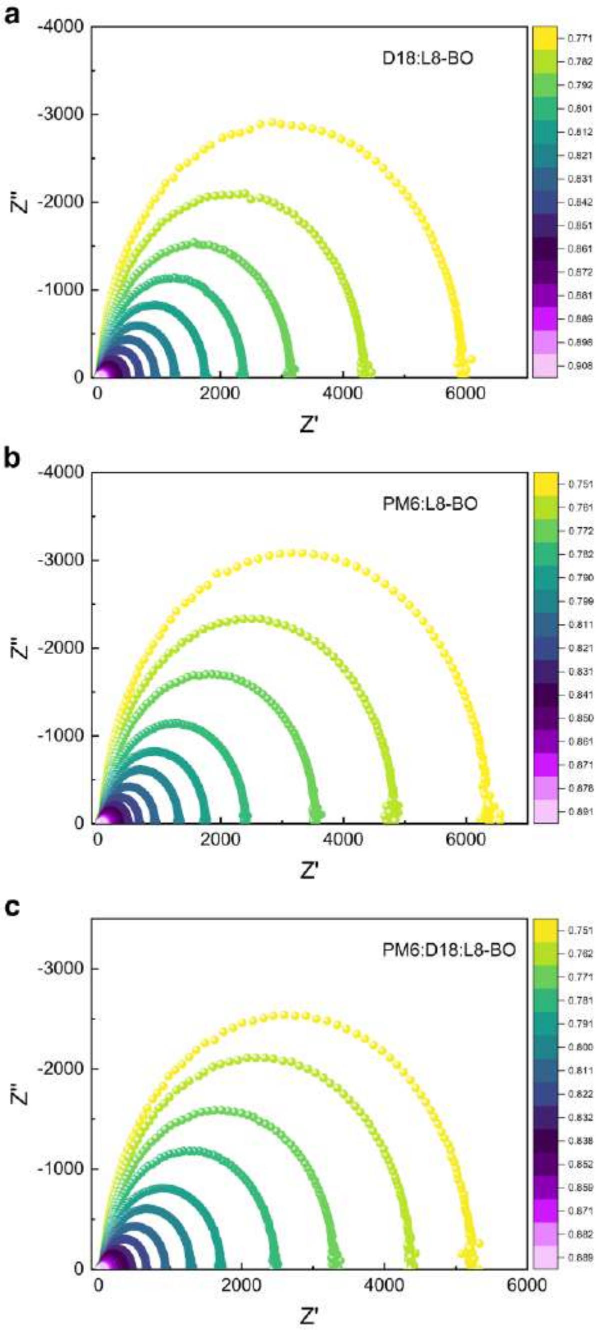

Supplementary Figure 28. The impedance spectra of binary and ternary devices measured under different light intensities.

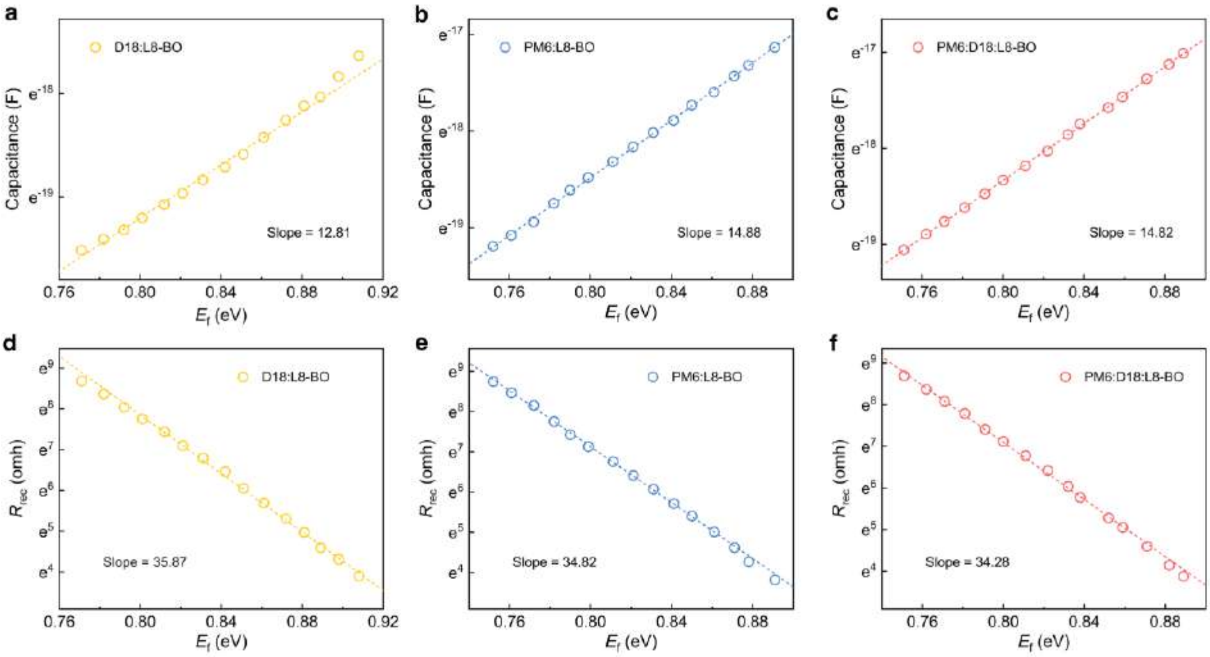

Supplementary Figure 29. The chemical capacitance (C_{μ}^{n}, a–c) and recombination resistance (R_{rec}, d–f) extracted from the low-frequency region of impedance spectra.

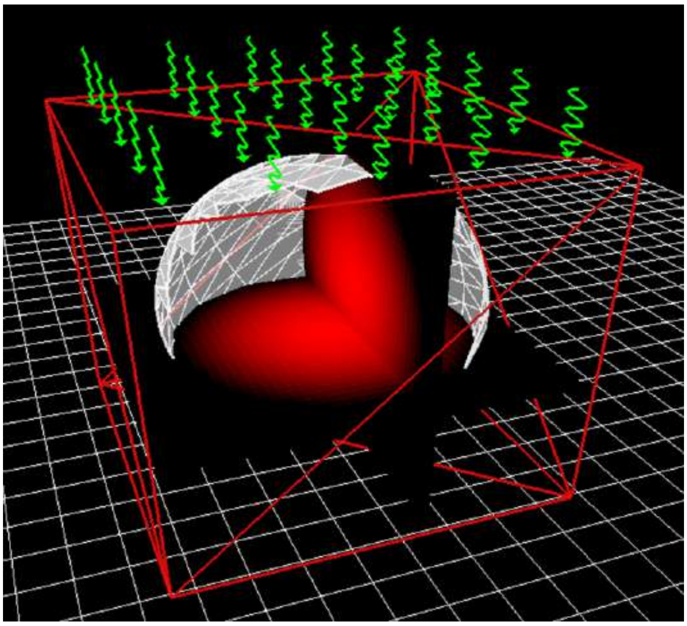

Supplementary Figure 30. 3D sphere for exciton diffusion simulations.

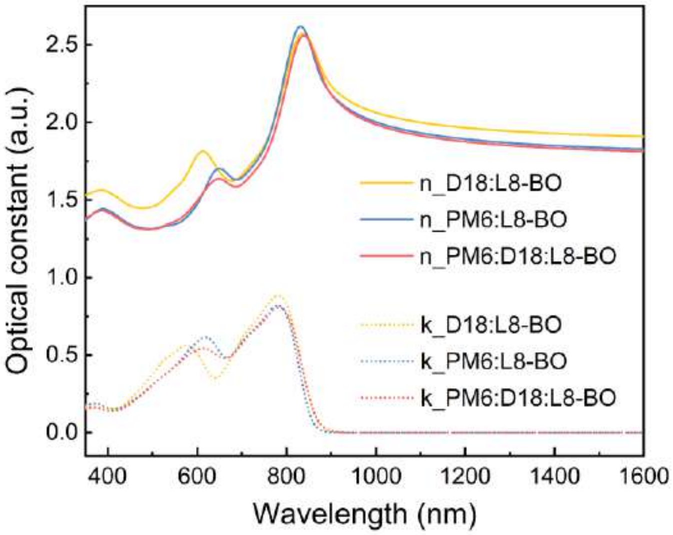

Supplementary Figure 31. Optical constants for D18:L8-BO, PM6:L8-BO, and PM6:D18:L8-BO blends, obtained from ellipsometry measurements.

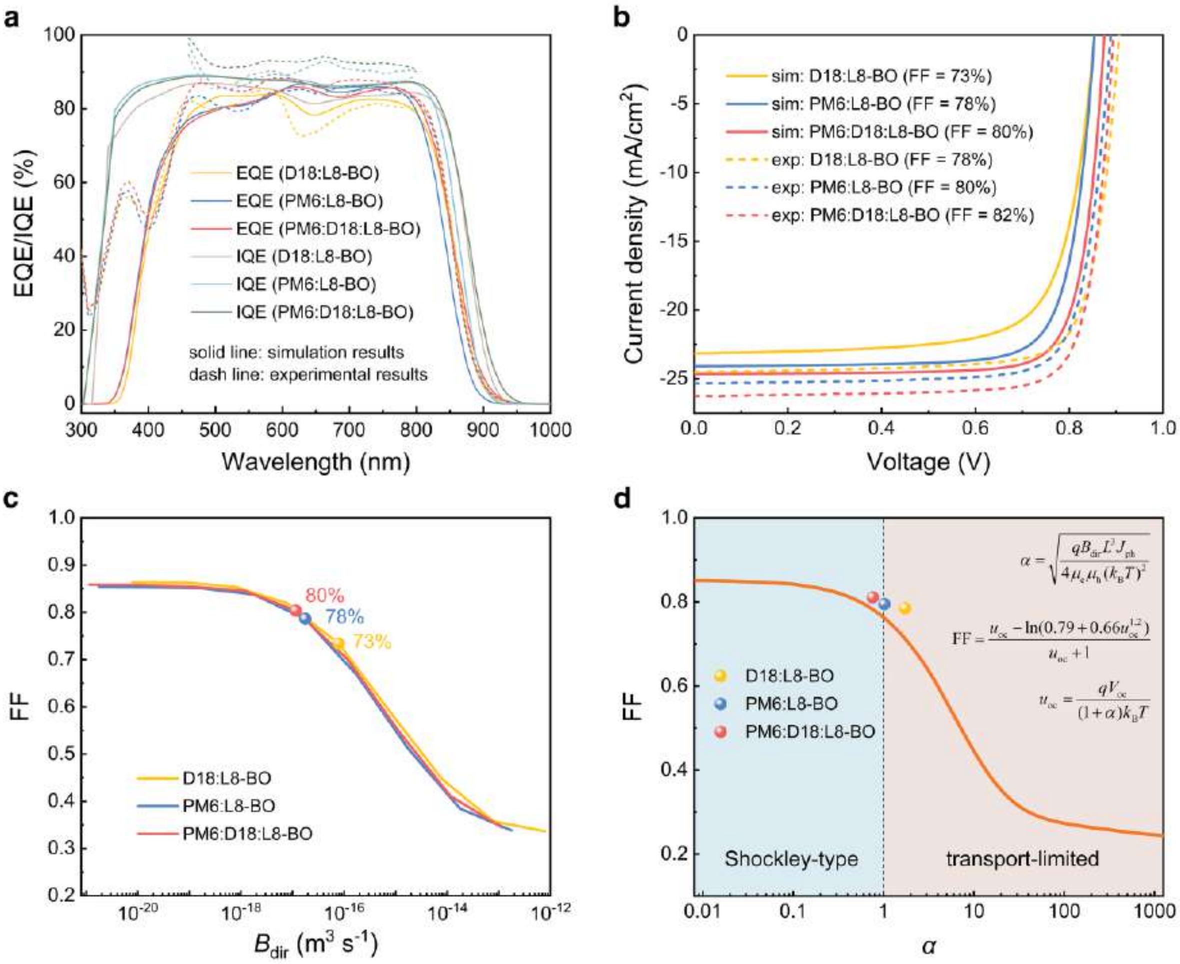

Supplementary Figure 32. Device simulation results. (a) Internal and external quantum efficiency (solid lines are simulation results, dashed lines are experimental results). (b) Simulated current–voltage characteristics (solid lines) as compared to experimental values (dashed lines). (c) Simulated FFs as a function of direct recombination coefficient (B_{dir}), and the values for each device are highlighted. (d) Figure-of-merit (α) on the competition between recombination and transport. Values for each device have been highlighted in the plots. The figure is adapted from reference[6].

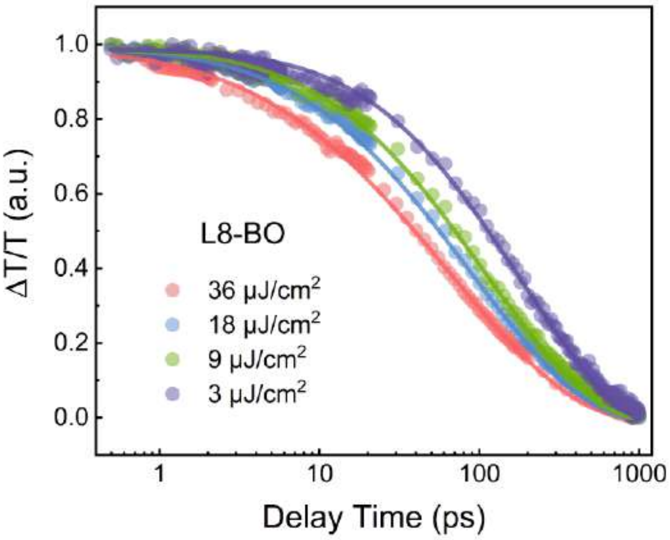

Supplementary Figure 33. The exciton decay kinetics of L8-BO neat film at indicated excitation fluences.

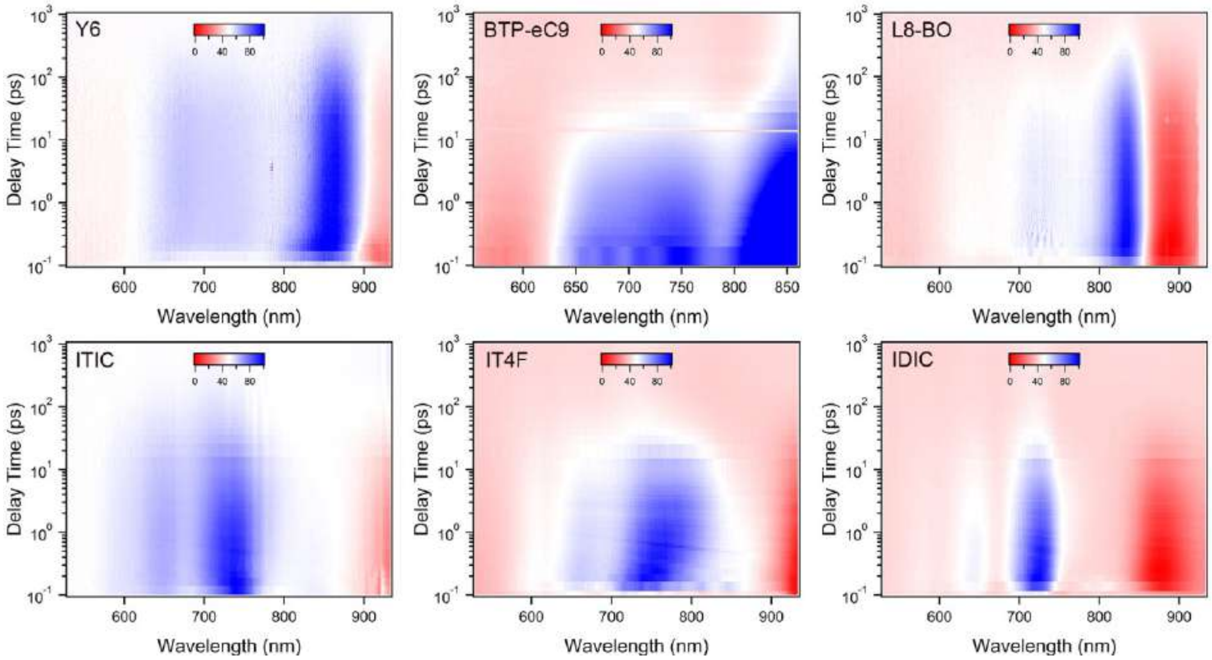

Supplementary Figure 34. The color plot of fs transient absorption spectra of different NFA films (Y6, BTP-eC9, L8-BO, ITIC, IT4F, and IDIC) under 750 nm excitation.

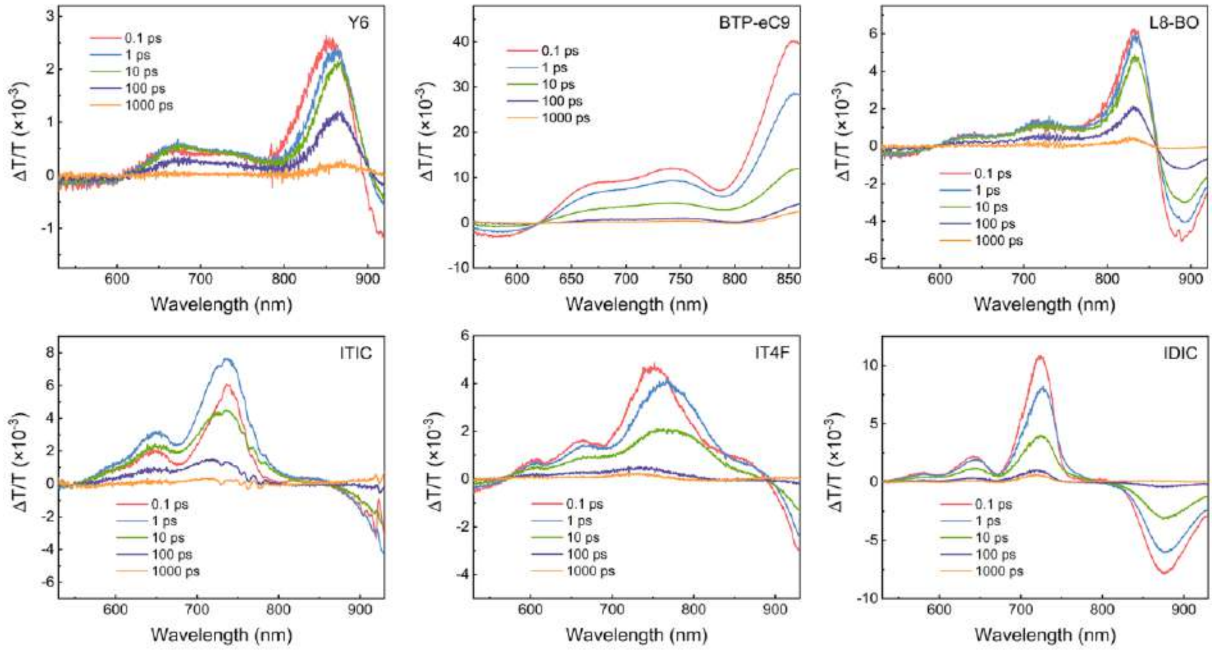

Supplementary Figure 35. The representative fs transient absorption spectra of different NFA films (Y6, BTP-eC9, L8-BO, ITIC, IT4F, and IDIC) at indicated delay times under 750 nm excitation.

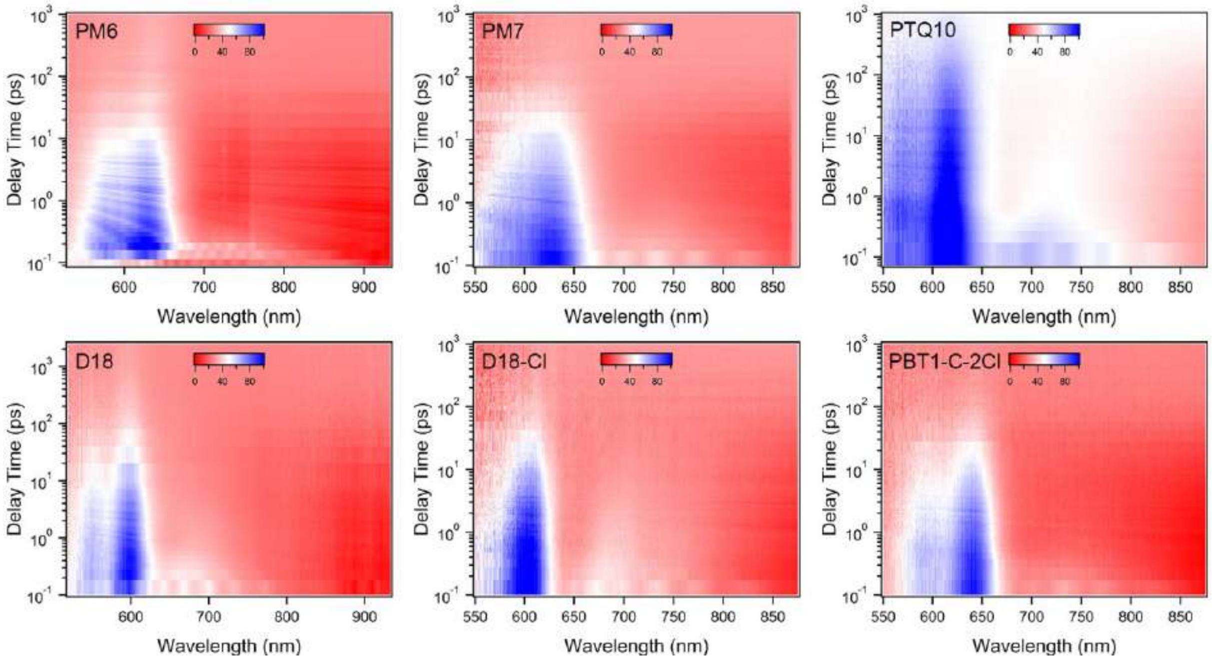

Supplementary Figure 36. The color plot of fs transient absorption spectra of different donor films (PM6, PM7, PTQ10, D18, D18-Cl, and PBT1-C-2Cl) under 750 nm excitation.

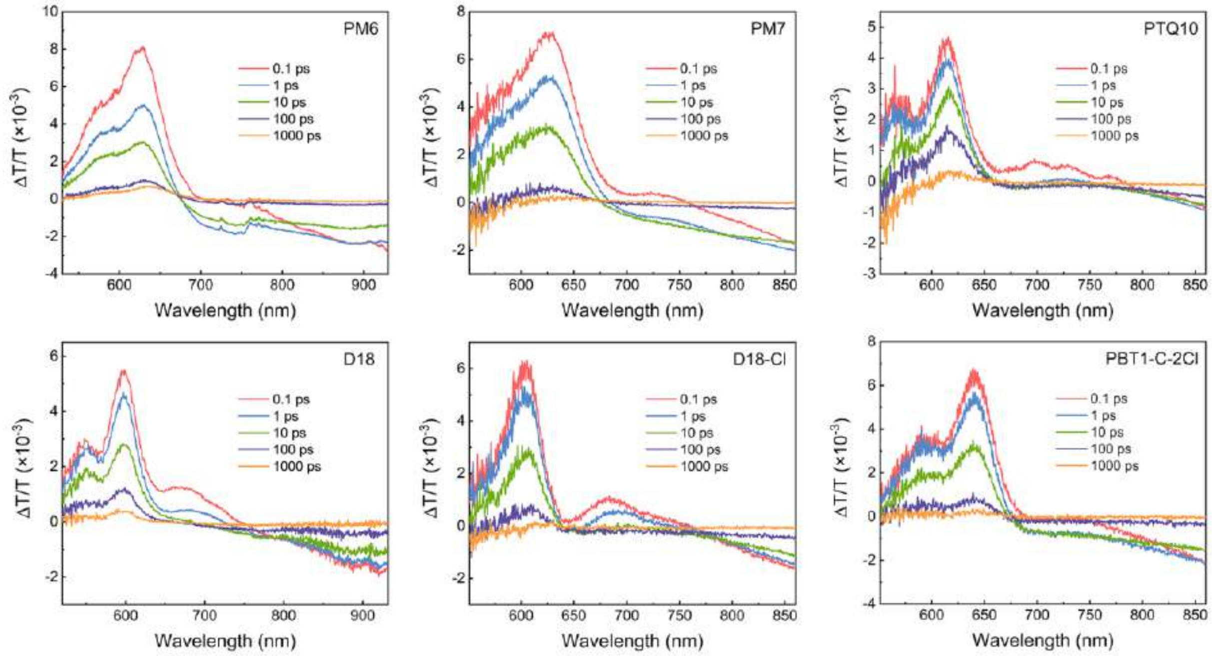

Supplementary Figure 37. The representative fs transient absorption spectra of different donor films (PM6, PM7, PTQ10, D18, D18-Cl, and PBT1-C-2Cl) at indicated delay times under 750 nm excitation.

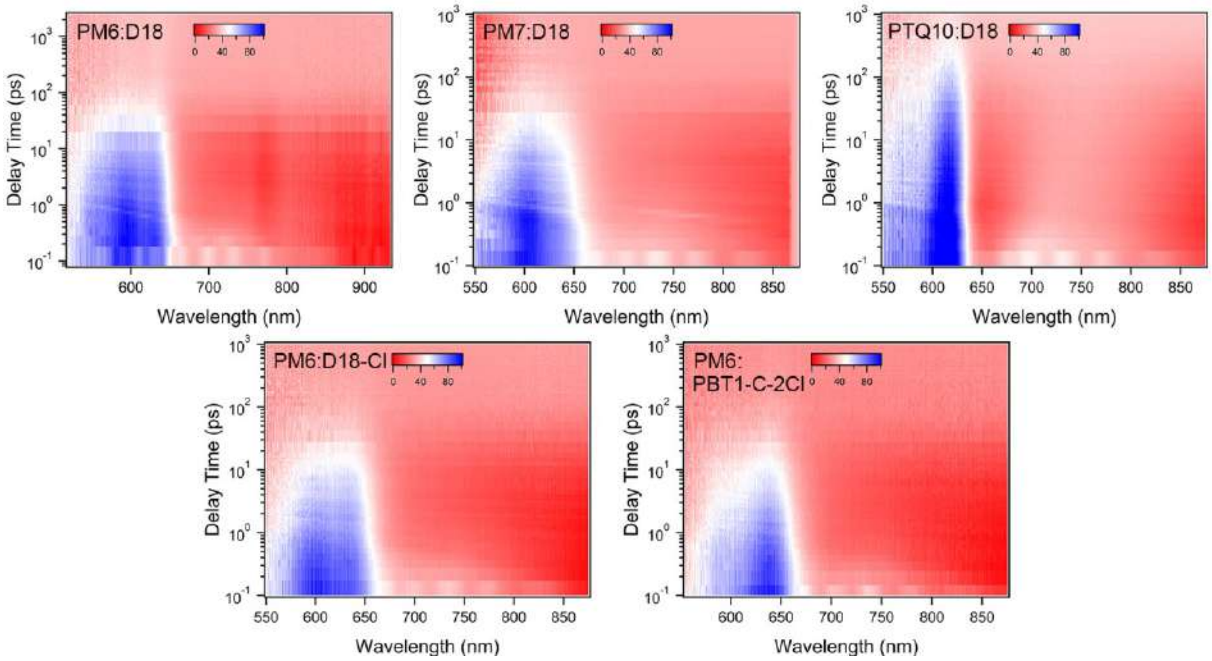

Supplementary Figure 38. The color plot of fs transient absorption spectra of different double blended donor films (PM6:D18=4:1, PM7:D18=4:1, PTQ10:D18=4:1, PM6:D18-Cl=4:1, and PM6:PBT1-C-2Cl=4:1) under 750 nm excitation.

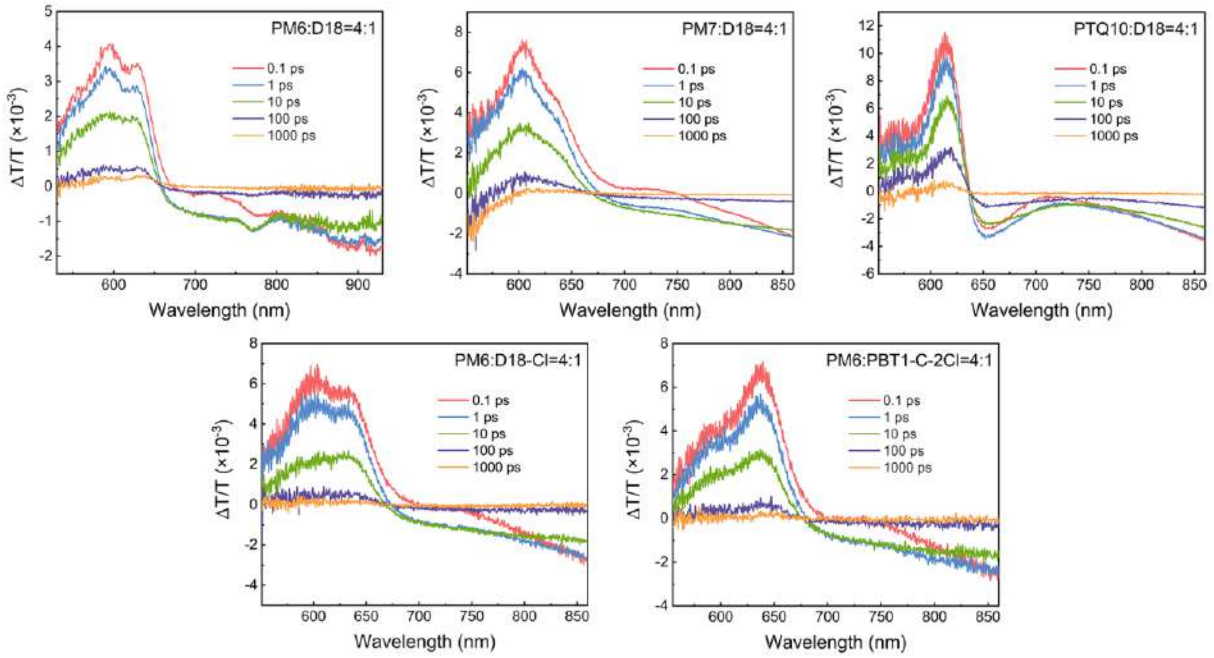

Supplementary Figure 39. The representative fs transient absorption spectra of different double blended donor films (PM6:D18=4:1, PM7:D18=4:1, PTQ10:D18=4:1, PM6:D18-Cl=4:1, and PM6:PBT1-C-2Cl=4:1) at indicated delay times under 750 nm excitation.

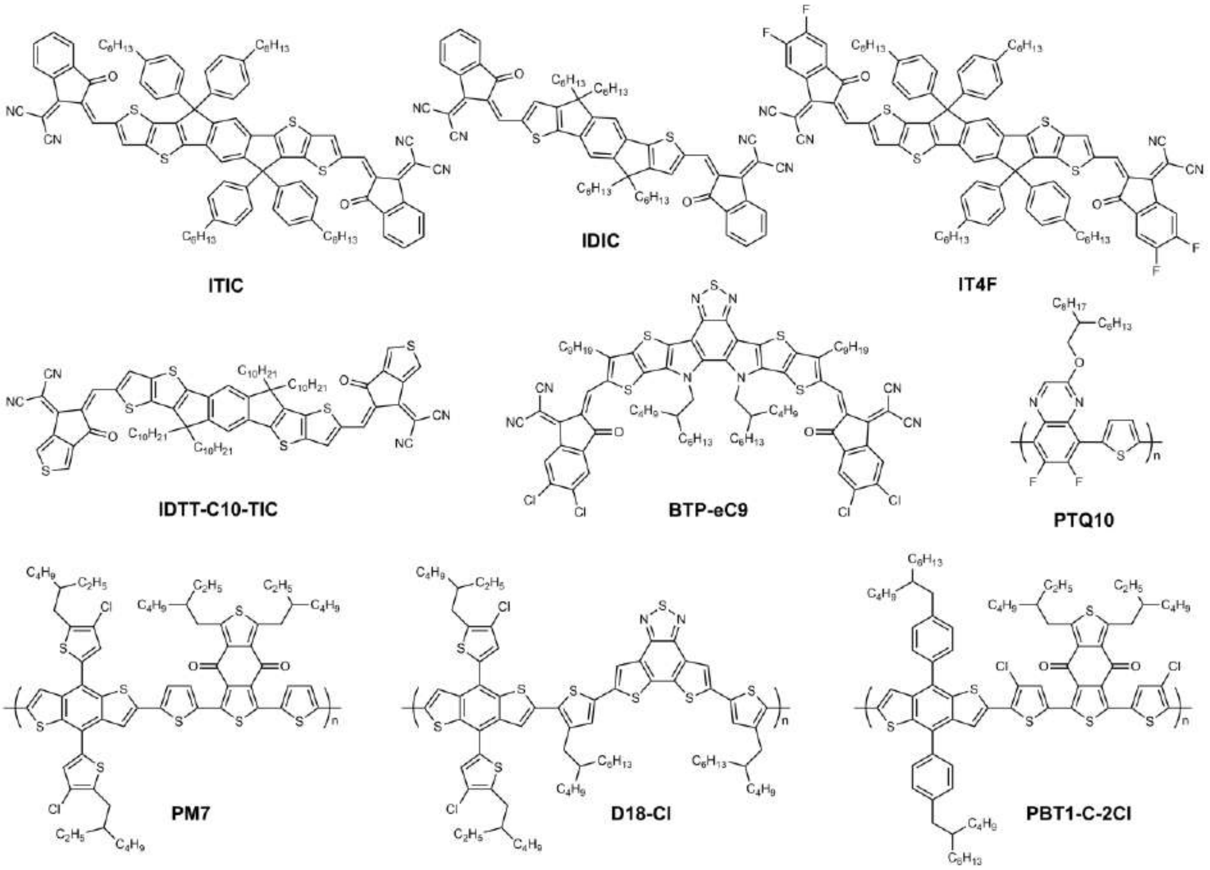

Supplementary Figure 40. Chemical structure of the donor and acceptor materials used in device fabrication.

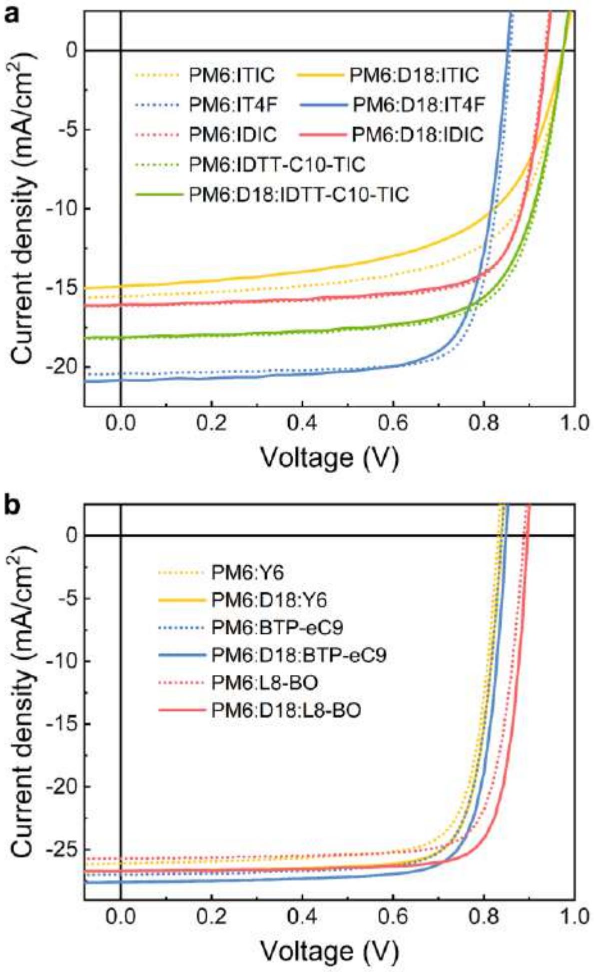

Supplementary Figure 41. *J–V* curves of binary and ternary OSCs with PM6 as the donor and different NFAs under the illumination of AM 1.5 G, 100 mW/cm^2 (the dotted line is for the binary device while the solid line is for the ternary device).

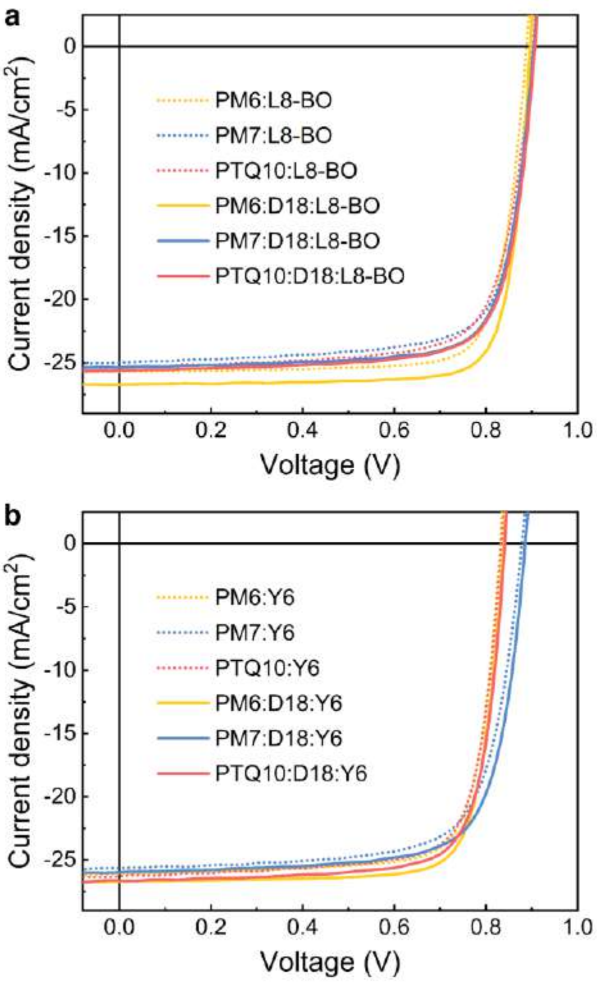

Supplementary Figure 42. *J–V* curves of binary and ternary OSCs with D18 as the secondary donor, L8-BO (a) and Y6 (b) as acceptor, and different primary donors (PM6, PM7, and PTQ10) under the illumination of AM 1.5 G, 100 mW/cm^2.

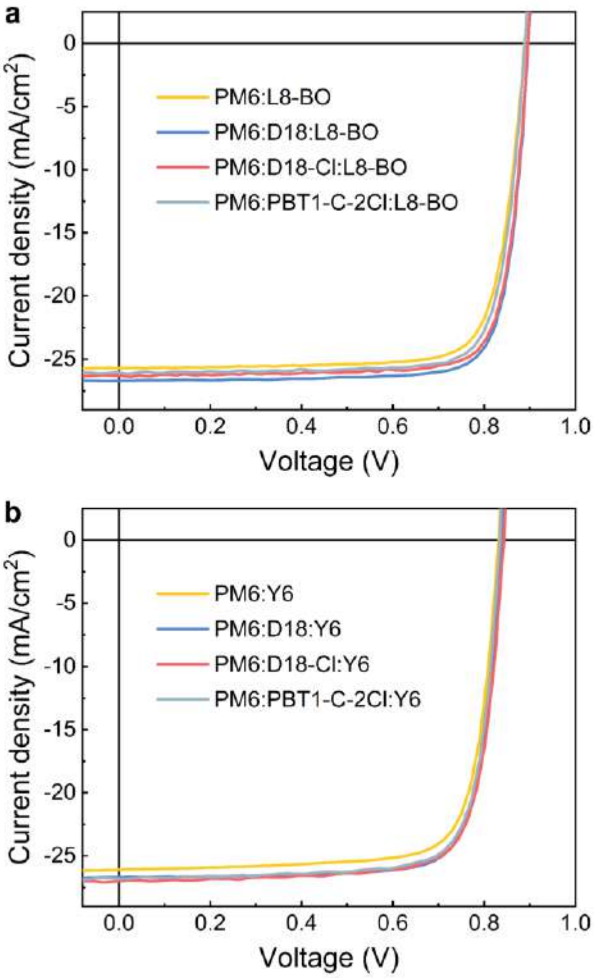

Supplementary Figure 43. *J–V* curves of binary and ternary OSCs with PM6 as the primary donor, L8-BO (a) and Y6 (b) as acceptor, and different secondary donors (D18, D18-Cl, and PBT1-C-2Cl) under the illumination of AM 1.5 G, 100 mW/cm^2.

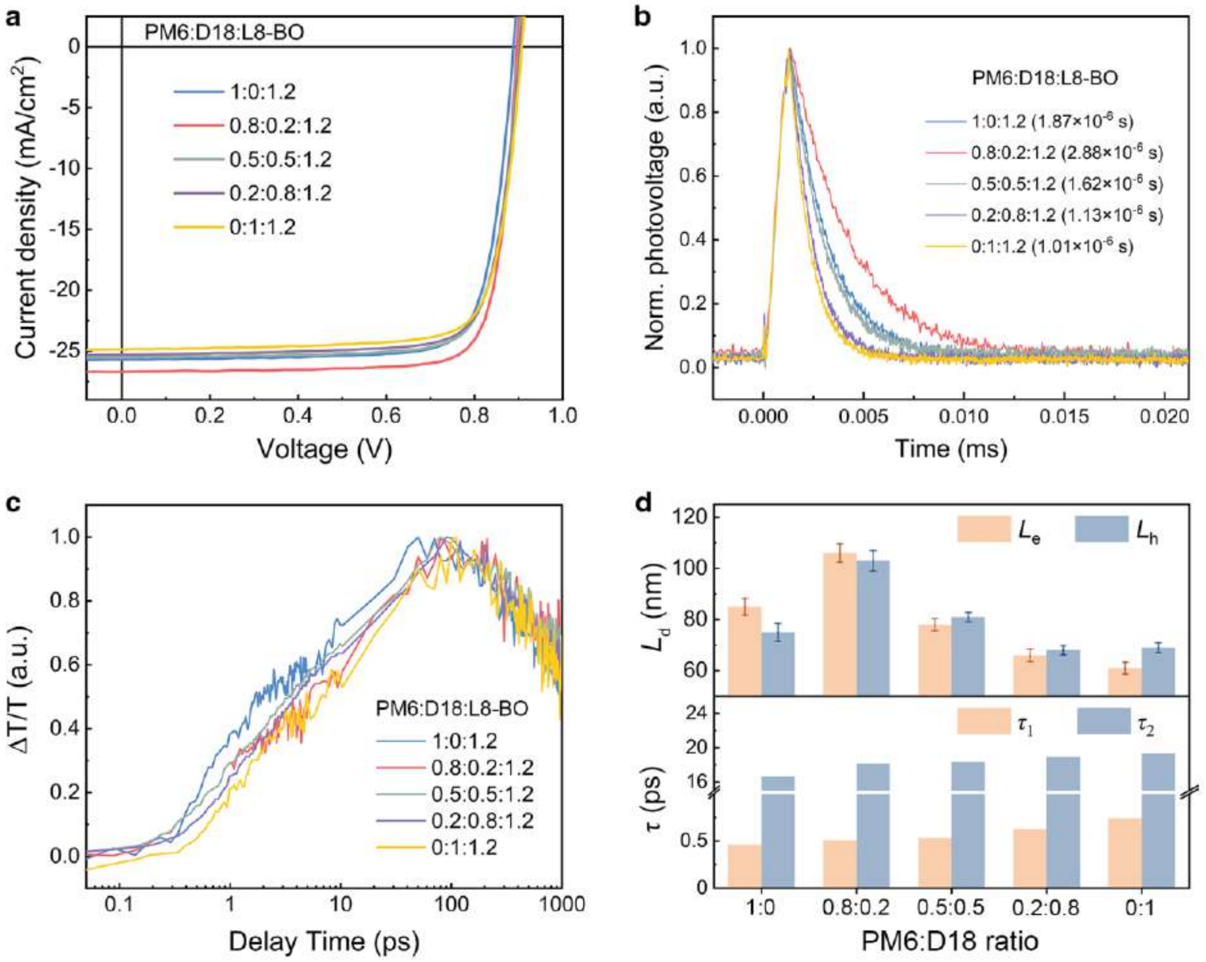

Supplementary Figure 44. (a) *J*–*V*, (b) TPV, and (c) TA curves, and (e) carrier diffusion length and the lifetime of hole transfer process under different blend conditions.

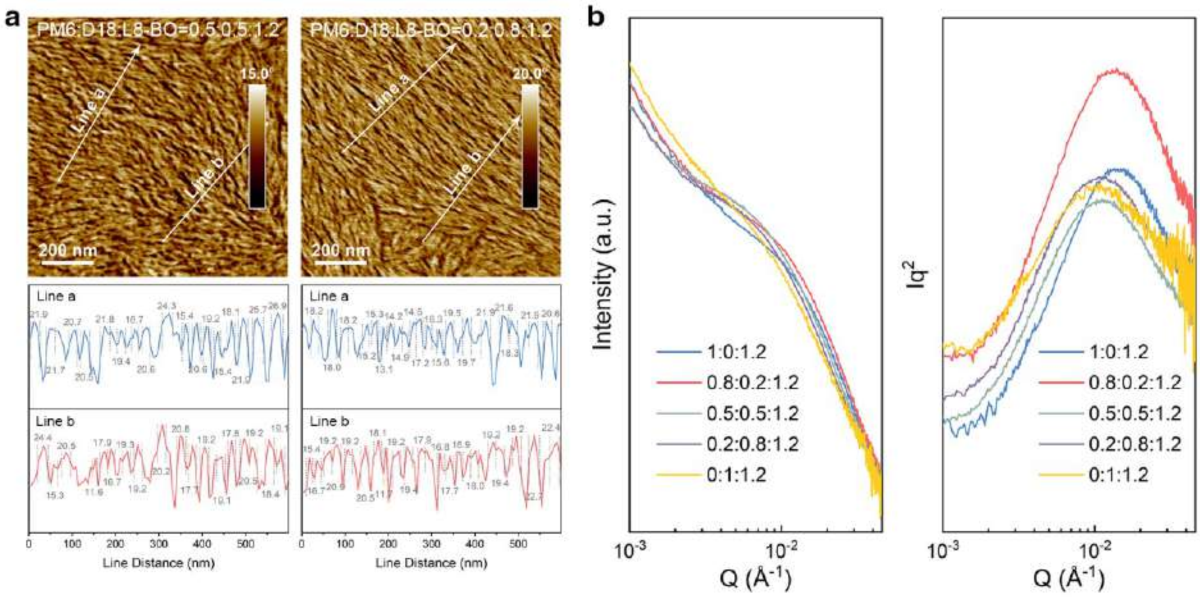

Supplementary Figure 45. AFM phase images of PM6:D18:L8-BO=0.5:0.5:1.2 and PM6:D18:L8-BO=0.2:0.8:1.2 blended films. The line profile to obtain the fibril diameter of both blended films, and the corresponding fibril diameters of PM6:D18:L8-BO=0.5:0.5:1.2 and PM6:D18:L8-BO=0.2:0.8:1.2 are 19.6 and 18.1 nm, respectively. (b) RSoXS profiles under 285.2 eV based on PM6:D18:L8-BO with different donor ratios.

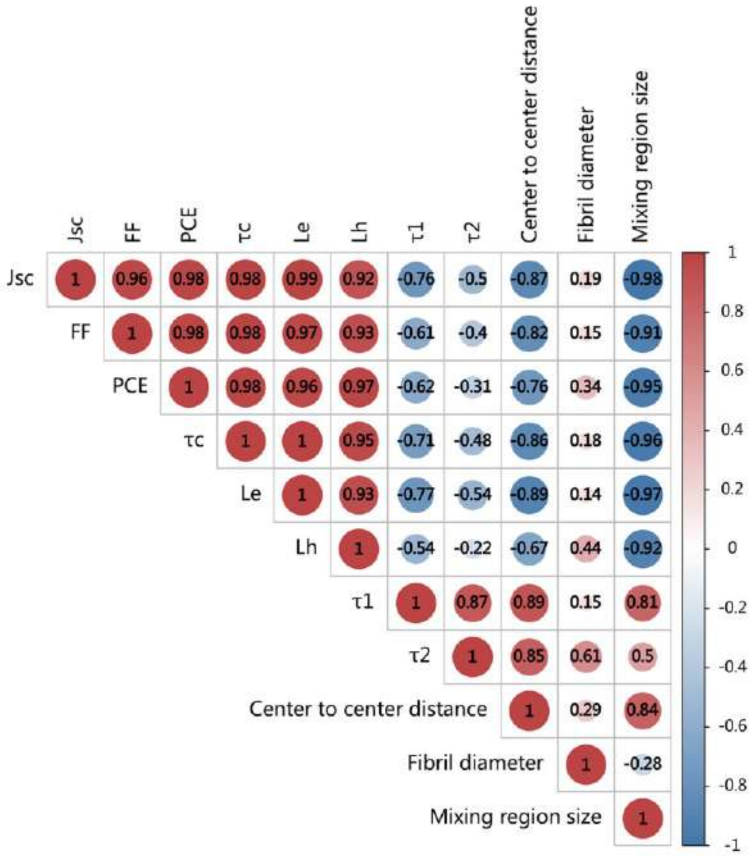

Supplementary Figure 46. Correlation matrix. Correlation of device, photophysics, and morphology characters (based on PM6:D18:L8-BO with different donor ratios). The photovoltaic, photophysical, and morphological characteristic parameters used in the correlation analysis are summarized in Supplementary Tables 18–20, and the detailed curves are summarized in Supplementary Figs. 44 and 45.

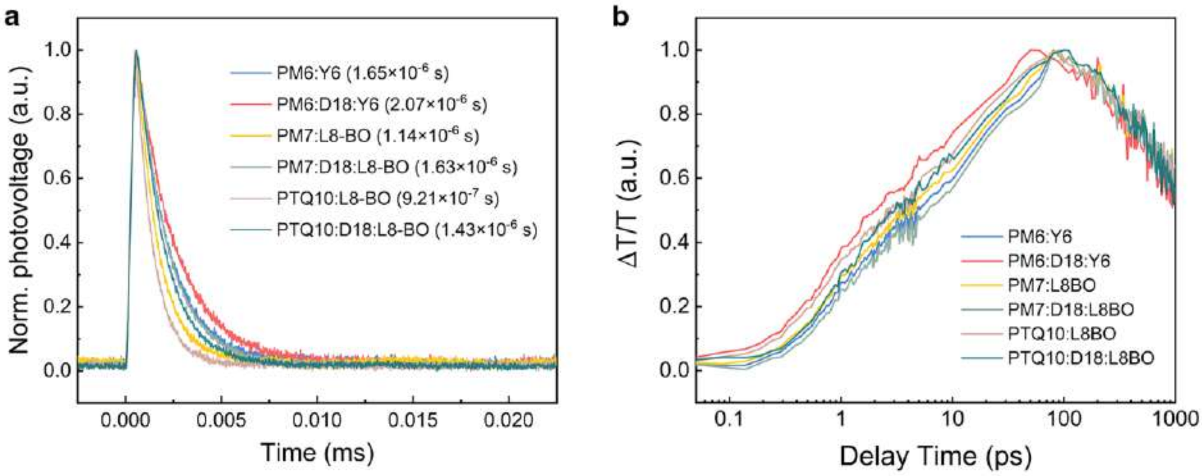

Supplementary Figure 47. (a) TPV, and (b) TA curves under different blend films.

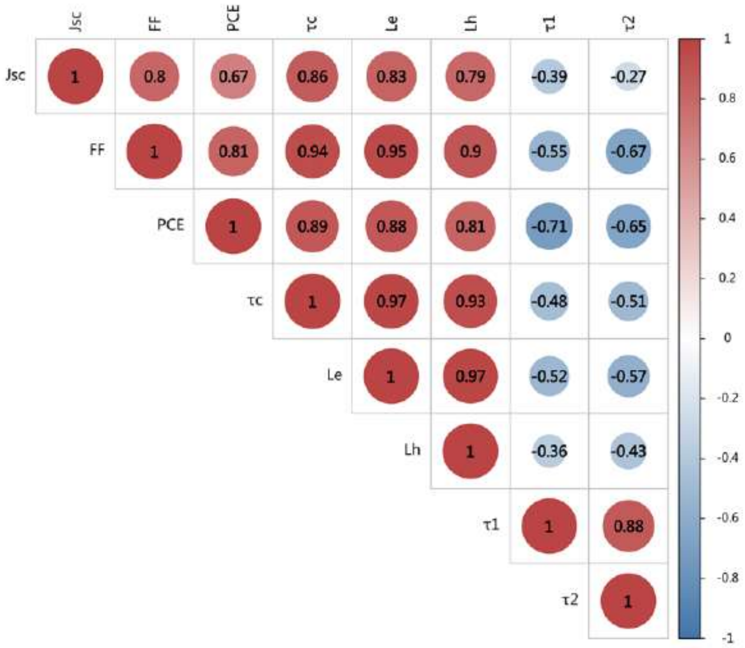

Supplementary Figure 48. Correlation matrix. Correlation of device and photophysics (based on PM6:L8-BO, PM6:D18:L8-BO, PM6:Y6, PM6:D18:Y6, PM7:L8-BO, PM7:D18:L8-BO, PTQ10:L8-BO, and PTQ10:D18:L8-BO). The photovoltaic and photophysical parameters used in the correlation analysis are summarized in Supplementary Table 21, and the detailed curves are summarized in Supplementary Fig. 47.

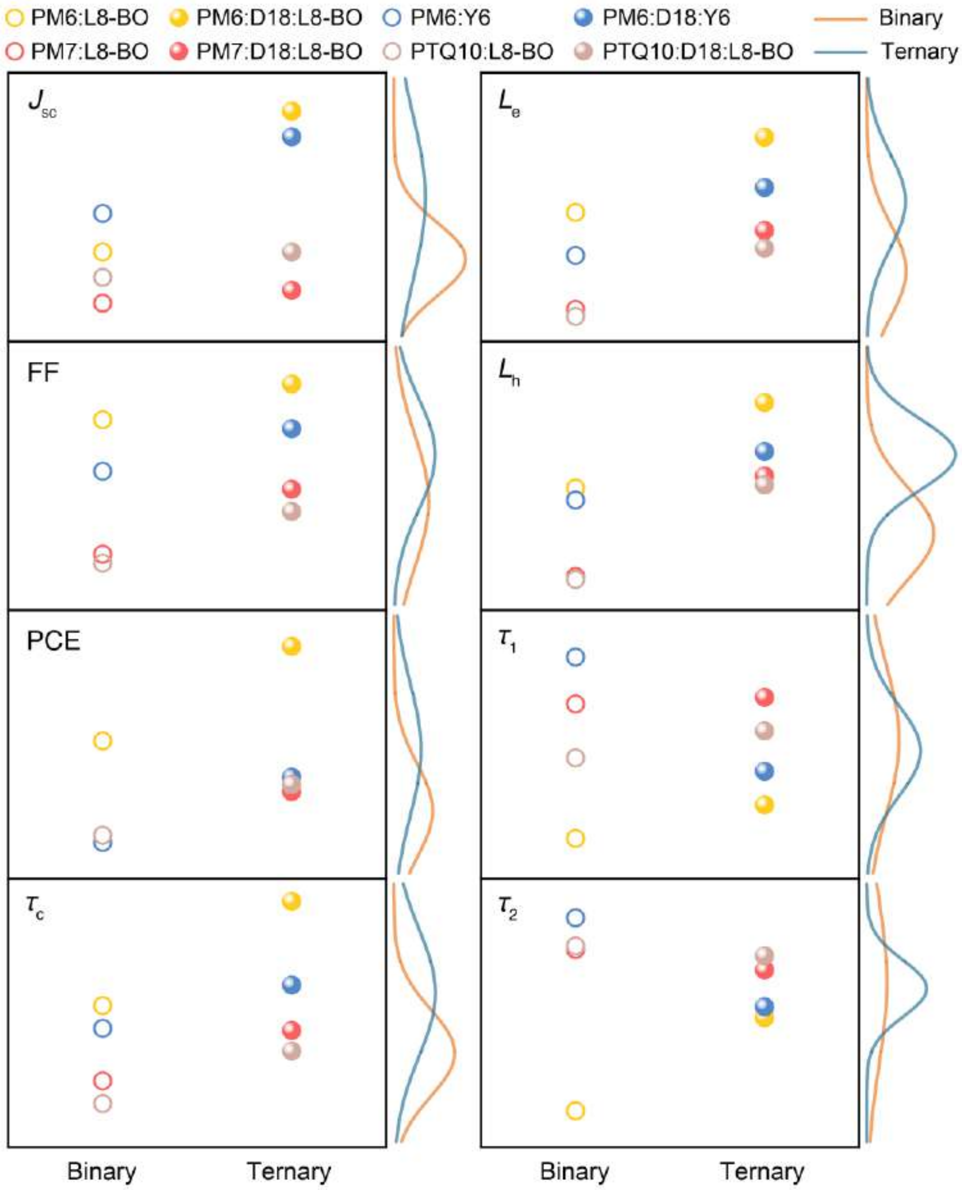

Supplementary Figure 49. Scatter diagram of photovoltaic (J_{sc}, FF, and PCE) and photophysical (τ_c, L_e, L_h, τ_1, and τ_2) parameters of binary and ternary devices. On the right are the distribution curves.

Supplementary Tables

Supplementary Table 1. Photovoltaic parameters with different PM6:D18 ratios for ternary devices under the illumination of AM 1.5 G, 100 mW/cm^2.

PM6:D18:L8-BO	V_{oc}^{a} (V)	J_{sc}^{a} (mA cm^{-2})	FF^a (%)	PCE^a (%)
0.9:0.1:1.2	0.892 (0.892 ± 0.001)	26.1 (25.8 ± 0.3)	80.2 (80.1 ± 0.7)	18.7 (18.45 ± 0.1)
0.7:0.3:1.2	0.898 (0.898 ± 0.001)	26.2 (25.9 ± 0.4)	81.0 (80.7 ± 0.6)	19.1 (18.8 ± 0.1)
0.5:0.5:1.2	0.901 (0.901 ± 0.001)	25.5 (25.2 ± 0.3)	79.4 (78.9 ± 0.8)	18.3 (18.0 ± 0.1)

[a] The average values are obtained from over 50 devices, with an aperture area of 3.2 mm^2. The values outside the parentheses denote the best optimal photovoltaic parameters, and the values inside the parentheses represent the average photovoltaic parameters and their standard deviations.

Supplementary Table 2. Structure parameters for different blend films. All three blend films show face-on orientation. Position, peak area, and FWHM are available through multi-peak fitting and *d*-spacing, CCL can be calculated by Scherrer Equation.

Blends	(010) *d*-spacing (Å)	(010) peak area	(010) CCL (Å)	(100) *d*-spacing (Å)	(100) peak area	(100) CCL (Å)
D18:L8-BO[a]	3.676	1128	20.03	20.59	295.1	146.8
PM6:L8-BO[a]	3.665	544.7	17.04	20.91	125.3	76.01
PM6:D18:L8-BO[b]	3.661	609.1	17.92	20.86	137.0	90.96

[a] 1:1.2 (weight ratio); [b] 0.8:0.2:1.2 (weight ratio).

Supplementary Table 3. Structure parameters for L8-BO (021) and D18 (001) peaks. Position, peak area, and FWHM are available through multi-peak fitting and *d*-spacing, CCL can be calculated by Scherrer Equation.

Blends	L8-BO (021) *d*-spacing (Å)	L8-BO (021) peak area	L8-BO (021) CCL (Å)	D18 (001) *d*-spacing (Å)	D18 (001) peak area	D18 (001) CCL (Å)
D18:L8-BO[a]	12.51	122.99	48.31	11.25	11.42	120.5
PM6:L8-BO[a]	12.57	93.02	25.82	-	-	-
PM6:D18:L8-BO[b]	12.66	101.54	34.74	11.30	2.88	107.7

[a] 1:1.2 (weight ratio); [b] 0.8:0.2:1.2 (weight ratio).

Supplementary Table 4. Fibril diameter and center to center distance and mixing region size of different blend films.

PM6:D18:L8-BO	q (Å^{-1})	Center to center distance (CCD, nm)	Fibril diameter (FD, nm)	Mixing region size (MRS, nm)[a]
0:1:1.2	0.0098	64.1	17.1	15.0
1:0:1.2	0.0131	47.8	14.3	9.6
0.8:0.2:1.2	0.0130	48.2	19.1	5.0

[a] $\mathrm{MRS} = \frac{\mathrm{CCD} - 2\mathrm{FD}}{2}$

Supplementary Table 5. Exciton diffusion length and lifetime in blend films (L_D is exciton diffusion length and τ is the lifetime of exciton).

Blends	Materials	Diffusion constant (cm^2/s)	L_D (nm)	τ (ps)
D18:L8-BO	D18	0.019	19.5	205
	L8-BO	0.043	39.4	360
PM6:L8-BO	PM6	0.026	13.3	69
	L8-BO	0.050	42.2	360
PM6:D18:L8-BO	PM6	0.032	14.9	69
	D18	0.022	21.4	205
	L8-BO	0.051	42.7	360

Supplementary Table 6. The lifetime of the hole transfer process in blend films. The data was achieved through the biexponential fitting.

Blends	τ_1 (ps)	τ_2 (ps)
D18:L8-BO[a]	0.74	19.30
PM6:L8-BO[a]	0.46	16.61
PM6:D18:L8-BO[b]	0.51	18.17

[a] 1:1.2 (weight ratio); [b] 0.8:0.2:1.2 (weight ratio).

Supplementary Table 7. Parameters of the dependence of photocurrent density (J_{ph}) on the effective voltage (V_{eff}).

Blends	V_{sat} (V)	J_{sat} (mA cm^{-2})	J_{sc} (mA cm^{-2})	J_{sc}/J_{sat}
D18:L8-BO[a]	0.172	24.8	24.5	0.988
PM6:L8-BO[a]	0.161	25.9	25.6	0.988
PM6:D18:L8-BO[b]	0.121	26.6	26.5	0.996

[a] 1:1.2 (weight ratio); [b] 0.8:0.2:1.2 (weight ratio).

Supplementary Table 8. Input parameters for SCLC mobility extractions using drift diffusion modelling using gpvdm under dark. The fitting parameters are highlighted in a yellow shade.

Parameters	Symbol	Values			Units
		D18:L8-BO	PM6:L8-BO	PM6:D18:L8-BO	
Temperature	T	300	300	300	K
Relative dielectric constant	ε_r	3	3	3	unitless
Effective density of states of free charges	N_C/N_V	1×10^{26}	1×10^{26}	1×10^{26}	m^{-3}
Generation rate	G	0 (dark)	0 (dark)	0 (dark)	$m^{-3}\ s^{-1}$
Free to free charge recombination coefficient	B_{dir}	7.86×10^{-17}	1.77×10^{-17}	1.15×10^{-17}	$m^3\ s^{-1}$
LUMO electron capture cross section	σ_e^e	1×10^{-15}	1×10^{-15}	1×10^{-15}	m^2
LUMO hole capture cross section	σ_h^e	1×10^{-20}	1×10^{-20}	1×10^{-20}	m^2
HOMO electron capture cross section	σ_e^h	1×10^{-20}	1×10^{-20}	1×10^{-20}	m^2
HOMO hole capture cross section	σ_h^h	1×10^{-15}	1×10^{-15}	1×10^{-15}	m^2
Effective band gap	E_g	1.32	1.28	1.29	eV
Active layer thickness	L	120	120	120	nm
Cathode injection barrier	φ_{cat}	Fitting parameters			eV
Anode injection barrier	φ_{an}	Fitting parameters			eV
Trap-Free Electron or hole mobility	$\mu_{e,h}$	Target			$cm^2\ V^{-1}s^{-1}$
Total electron or hole trap density	$U_{n,p}^{Gau}$	3.76×10^{21}	7.04×10^{21}	5.68×10^{21}	m^{-3}
Trap centre depth relative to band	$D_{n,p}^{Gau}$	0.164	0.174	0.17	eV
Gaussian width of trap states	$\sigma_{n,p}^{Gau}$	0.018	0.022	0.021	eV

Supplementary Table 9. Extracted mobility values from drift diffusion modelling using gpvdm.

Parameters-Electron mobility	Symbol	Values			Units
		D18:L8-BO	PM6:L8-BO	PM6:D18:L8-BO	
Cathode injection barrier	φ_{cat}	0.00	0.00	0.00	eV
Anode injection barrier	φ_{an}	0.31	0.27	0.31	eV
Trap-free electron mobility	μ_e	1.40×10^{-3}	1.50×10^{-3}	1.49×10^{-3}	$\mathrm{cm^2\ V^{-1}s^{-1}}$

Parameters-Hole mobility	Symbol	Values			Units
		D18:L8-BO	PM6:L8-BO	PM6:D18:L8-BO	
Cathode injection barrier	φ_{cat}	0.32	0.34	0.33	eV
Anode injection barrier	φ_{an}	0.00	0.00	0.00	eV
Trap-free hole mobility	μ_h	1.80×10^{-3}	1.15×10^{-3}	1.42×10^{-3}	$\mathrm{cm^2\ V^{-1}s^{-1}}$

Supplementary Table 10. The carrier mobility, carrier diffusion length, and carrier drift length of the device under different conditions.

Blends	μ_e[a] (cm^2 V^{-1} s^{-1})	μ_h[a] (cm^2 V^{-1} s^{-1})	L_e[b] (nm)	L_h[b] (nm)	$L_{dr,e}$[c] (nm)	$L_{dr,h}$[c] (nm)
D18:L8-BO[b]	$(1.40 \pm 0.11) \times 10^{-3}$	$(1.80 \pm 0.10) \times 10^{-3}$	61 ± 2.3	69 ± 1.9	940	1209
PM6:L8-BO[b]	$(1.50 \pm 0.12) \times 10^{-3}$	$(1.15 \pm 0.12) \times 10^{-3}$	85 ± 3.3	75 ± 3.5	1767	1355
PM6:D18:L8-BO[c]	$(1.49 \pm 0.12) \times 10^{-3}$	$(1.42 \pm 0.13) \times 10^{-3}$	106 ± 3.6	103 ± 4.0	2732	2604

[a] The average parameters were calculated from 5 devices; [b] 1:1.2 (weight ratio); [c] 0.8:0.2:1.2 (weight ratio). L_e and L_h represent electron and hole diffusion lengths respectively.

[b] $L_d = \sqrt{\frac{k_B T}{q} \cdot \mu\tau}$ (L_d is the carrier diffusion length, k_B is the Boltzmann constant, T is the temperature, q is the elementary charge, μ is the carrier mobility, τ is the charge carrier lifetime).

[c] $L_{dr} = \frac{\mu\tau V_{bi}}{d}$ (L_{dr} is the carrier drift length, μ is the carrier mobility, τ is the charge carrier lifetime, V_{bi} is the built-in voltage).

Supplementary Table 11. The parameters derived from the impedance spectroscopy measurement.

Blends	V_{oc} (V)	J_{sc} (mA cm^{-2})	N (cm^{-3})	$U_{\mathrm{n,p}}^{\mathrm{Gau}}$ / N	δ (meV)	β/α
D18:L8-BO	0.907	24.9	2.38×10^{19}	1.58×10^{-4}	66.8	2.80
PM6:L8-BO	0.888	25.7	5.31×10^{19}	1.33×10^{-4}	67.5	2.34
PM6:D18:L8-BO	0.896	26.7	6.30×10^{19}	9.02×10^{-5}	67.1	2.31

Supplementary Table 12. Parameters for 3D exciton diffusion modelling. Values are taken from L8-BO in blends in Supplementary Table 5.

Blends	Diffusion constant (cm^2/s)	L_D (nm)	τ (ps)	k_{diss} (ps^{-1})	Phase separation scales of L8-BO (nm)	Exciton diffusion efficiency (%)
D18:L8-BO	0.043	39.4	360	1.35	68.8	93.74
PM6:L8-BO	0.050	42.2	360	2.17	49.0	96.87
PM6:D18:L8-BO	0.051	42.7	360	1.96	51.8	96.64

Note: Yellow shade area is the calculated exciton diffusion efficiency for each blend.

Supplementary Table 13. Input parameters for drift diffusion modelling using gpvdm at 1 sun illumination.

Parameters	Symbol	Values			Units
		D18:L8-BO	PM6:L8-BO	PM6:D18:L8-BO	
Temperature	T	300	300	300	K
Relative dielectric constant	ε_r	3	3	3	unitless
Effective density of states of free charges	N_C/N_V	1×10^{26}	1×10^{26}	1×10^{26}	m^{-3}
Generation rate	G	Calculated using coupled exciton diffusion and optical models			$m^{-3}\ s^{-1}$
Free to free charge recombination coefficient	B_{dir}	7.86×10^{-17}	1.77×10^{-17}	1.15×10^{-17}	$m^3\ s^{-1}$
Effective band gap	E_g	1.32	1.28	1.29	eV
Active layer thickness	L	120	120	120	nm
Cathode injection barrier	φ_{cat}	0.01	0.01	0.01	eV
Anode injection barrier	φ_{an}	0.01	0.01	0.01	eV
Electron mobility	μ_e	1.40×10^{-3}	1.50×10^{-3}	1.49×10^{-3}	$cm^2\ V^{-1}s^{-1}$
Hole mobility	μ_h	1.80×10^{-3}	1.15×10^{-3}	1.42×10^{-3}	$cm^2\ V^{-1}s^{-1}$

Supplementary Table 14. Exciton diffusion length and lifetime in donor or acceptor neat films (L_D is exciton diffusion length and τ is the lifetime of exciton).

Materials	Diffusion constant (cm^2/s)	L_D (nm)	τ (ps)
$PC_{61}BM$	-	5.1[7]	-
$PC_{71}BM$	-	3.0[8]	-
ITIC	0.014	13.2	125
IT4F	0.015	13.5	120
IDIC	0.020	19.5	190
Y6	0.052	39.5	300
BTP-eC9	0.037	33.1	295
L8-BO	0.050	43.0	360
PM6	0.027	13.6	69.1
PM7	0.024	13.5	76
PTQ10	0.024	13.1	72
D18	0.030	24.7	205
D18-Cl	0.029	23.6	193
PBT1-C-2Cl	0.026	15.4	95
PM6:D18=4:1	0.028	18.9	125
PM7:D18=4:1	0.028	17.9	115
PTQ10:D18=4:1	0.029	17.6	108
PM6:D18-Cl=4:1	0.025	18.2	133
PM6:PBT1-C-2Cl=4:1	0.025	14.5	83

Supplementary Table 15. Photovoltaic parameters of binary and ternary OSCs with PM6 as the primary donor and different NFAs under the illumination of AM 1.5 G, 100 mW/cm^2.

Blends	V_{oc}[a] (V)	J_{sc}[a] (mA cm^{-2})	FF[a] (%)	PCE[a] (%)
PM6:ITIC[b,f]	0.976 (0.974 ± 0.001)	15.6 (15.6 ± 0.2)	64.8 (63.8 ± 0.7)	9.84 (9.70 ± 0.08)
PM6:D18:ITIC[c,f]	0.974 (0.975 ± 0.002)	14.9 (14.6 ± 0.4)	59.1 (58.5 ± 1.0)	8.58 (8.32 ± 0.14)
PM6:IT4F[b,f]	0.858 (0.855 ± 0.002)	20.4 (20.4 ± 0.3)	78.8 (77.7 ± 0.7)	13.8 (13.5 ± 0.2)
PM6:D18:IT4F[c,f]	0.852 (0.855 ± 0.002)	20.8 (20.4 ± 0.3)	75.3 (75.5 ± 0.6)	13.4 (13.2 ± 0.1)
PM6:IDIC[b,g]	0.935 (0.935 ± 0.003)	16.2 (15.7 ± 0.3)	75.4 (75.9 ± 0.6)	11.4 (11.1 ± 0.2)
PM6:D18:IDIC[c,g]	0.938 (0.936 ± 0.002)	16.1 (15.8 ± 0.2)	74.7 (75.0 ± 0.5)	11.3 (11.1 ± 0.1)
PM6:IDTT-C10-TIC[d,h]	0.975 (0.974 ± 0.001)	18.2 (18.0 ± 0.2)	71.8 (72.0 ± 0.6)	12.8 (12.6 ± 0.1)
PM6:D18:IDTT-C10-TIC[e,h]	0.974 (0.974 ± 0.002)	18.1 (17.9 ± 0.2)	70.6 (70.5 ± 0.5)	12.5 (12.3 ± 0.1)
PM6:Y6[d,i]	0.832 (0.831 ± 0.001)	26.1 (25.8 ± 0.3)	77.6 (77.2 ± 0.4)	16.9 (16.6 ± 0.2)
PM6:D18:Y6[e,i]	0.839 (0.838 ± 0.001)	26.7 (26.4 ± 0.2)	79.1 (79.1 ± 0.4)	17.7 (17.5 ± 0.2)
PM6:BTP-eC9[d,j]	0.840 (0.840 ± 0.001)	27.0 (26.5 ± 0.4)	78.3 (78.2 ± 0.6)	17.7 (17.4 ± 0.2)
PM6:D18:BTP-eC9[e,j]	0.848 (0.848 ± 0.001)	27.6 (27.2 ± 0.4)	79.4 (79.1 ± 0.6)	18.6 (18.2 ± 0.2)
PM6:L8-BO[d,k]	0.888 (0.888 ± 0.001)	25.7 (25.5 ± 0.3)	79.9 (79.5 ± 1.1)	18.2 (18.0 ± 0.1)
PM6:D18:L8-BO[e,k]	0.896 (0.896 ± 0.001)	26.7 (26.6 ± 0.3)	81.9 (81.1 ± 0.8)	19.6 (19.3 ± 0.1)

[a] The average values are obtained from 20 devices, with an aperture area of 3.2 mm^2. The values outside the parentheses denote the best optimal photovoltaic parameters, and the values inside the parentheses represent the average photovoltaic parameters and their standard deviations. [b] D:A=1:1 (weight ratio); [c] D1:D2:A=0.8:0.2:1 (weight ratio); [d] D:A=1:1.2 (weight ratio); [e] D1:D2:A=0.8:0.2:1.2 (weight ratio). [f] The device architecture is ITO/PEDOT:PSS/active layer/PFN-Br/Ag; donor concentration = 10 mg mL^{-1} in CB with 0.75% DIO, following with 100 °C TA treatment for 10 min. [g] The device architecture is ITO/PEDOT:PSS/active layer/PFN-Br/Ag; donor concentration = 10 mg mL^{-1} in CB. [h] The device architecture is ITO/PEDOT:PSS/active layer/PFN-Br/Ag; donor concentration = 6.5 mg mL^{-1} in CF with 0.5% DIO, following with 85 °C TA treatment for 5 min. [i] The device architecture is ITO/PEDOT:PSS/active layer/PNDIT-F3N/Ag; donor concentration = 6.5 mg mL^{-1} in CF with 0.5% 1-CN, following with 85 °C TA treatment for 5 min. [j] The device architecture is ITO/PEDOT:PSS/active layer/PNDIT-F3N/Ag; donor concentration = 6.5 mg mL^{-1} in CF with 0.5% DIO, following with 85 °C TA treatment for 5 min. [k] The device architecture is ITO/PEDOT:PSS/active layer/PNDIT-F3N/Ag; donor concentration = 6.5 mg mL^{-1} in CF with DIB as solid additive (the content of DIB is 50% of the total mass of donor and acceptor), following with 85 °C TA treatment for 5 min.

Supplementary Table 16. Photovoltaic parameters of binary and ternary OSCs with D18 as the secondary donor, Y6 and L8-BO as acceptor, and different primary donors (PM6, PM7, and PTQ10) under the illumination of AM 1.5 G, 100 mW/cm^2.

Donor 1	Donor 2	Acceptor	V_{oc}[a] (V)	J_{sc}[a] (mA cm^{-2})	FF[a] (%)	PCE[a] (%)
PM6	-	Y6[b,d,g]	0.832 (0.831 ± 0.001)	26.1 (25.8 ± 0.3)	77.6 (77.2 ± 0.4)	16.9 (16.6 ± 0.2)
PM7	-	Y6[b,d,h]	0.880 (0.879 ± 0.002)	25.7 (25.7 ± 0.2)	72.3 (70.6 ± 1.4)	16.3 (16.0 ± 0.2)
PTQ10	-	Y6[b,e,i]	0.833 (0.833 ± 0.002)	26.3 (26.1 ± 0.3)	76.1 (75.8 ± 0.9)	16.7 (16.5 ± 0.1)
PM6	-	L8-BO[b,f,g]	0.888 (0.888 ± 0.001)	25.7 (25.5 ± 0.3)	79.9 (79.5 ± 1.1)	18.2 (18.0 ± 0.1)
PM7	-	L8-BO[b,f,h]	0.906 (0.906 ± 0.002)	25.0 (25.1 ± 0.4)	75.0 (73.5 ± 1.6)	17.0 (16.7 ± 0.2)
PTQ10	-	L8-BO[b,f,i]	0.902 (0.901 ± 0.002)	25.3 (25.3 ± 0.4)	74.4 (73.1 ± 1.3)	17.0 (16.7 ± 0.2)
PM6	D18	Y6[c,d,g]	0.839 (0.838 ± 0.001)	26.7 (26.4 ± 0.2)	79.1 (79.1 ± 0.4)	17.7 (17.5 ± 0.2)
PM7	D18	Y6[c,d,h]	0.886 (0.886 ± 0.001)	26.0 (25.9 ± 0.3)	74.2 (73.1 ± 1.3)	17.1 (16.8 ± 0.2)
PTQ10	D18	Y6[c,e,i]	0.841 (0.840 ± 0.002)	26.6 (26.6 ± 0.4)	77.0 (75.8 ± 1.1)	17.3 (17.0 ± 0.2)
PM6	D18	L8-BO[c,f,g]	0.896 (0.896 ± 0.001)	26.7 (26.6 ± 0.3)	81.9 (81.1 ± 0.8)	19.6 (19.3 ± 0.1)
PM7	D18	L8-BO[c,f,h]	0.904 (0.904 ± 0.002)	25.4 (25.2 ± 0.4)	76.8 (76.4 ± 1.0)	17.6 (17.3 ± 0.2)
PTQ10	D18	L8-BO[c,f,i]	0.906 (0.906 ± 0.002)	25.6 (25.5 ± 0.4)	76.1 (75.4 ± 0.9)	17.7 (17.4 ± 0.2)

[a]The average values are obtained from 20 devices, with an aperture area of 3.2 mm^2. The values outside the parentheses denote the best optimal photovoltaic parameters, and the values inside the parentheses represent the average photovoltaic parameters and their standard deviations. [b]D:A=1:1.2 (weight ratio); [c]D1:D2:A=0.8:0.2:1.2 (weight ratio). [d]0.5% 1-CN (v/v); [e]0.25% DIO (v/v); [f]DIB (the content of DIB is 50% of the total mass of donor and acceptor). [g]The device architecture is ITO/PEDOT:PSS/active layer/PNDIT-F3N/Ag; donor concentration = 6.5 mg mL^{-1} in CF, following with 85 °C TA treatment for 5 min. [h]The device architecture is ITO/PEDOT:PSS/active layer/PNDIT-F3N/Ag; donor concentration = 7.5 mg mL^{-1} in CF, following with 100 °C TA treatment for 10 min. [i]The device architecture is ITO/PEDOT:PSS/active layer/PNINN/Ag; donor concentration = 7.5 mg mL^{-1} in CF, following with 100 °C TA treatment for 10 min.

Supplementary Table 17. Photovoltaic parameters of binary and ternary OSCs with PM6 as the primary donor, Y6 and L8-BO as acceptor, and different secondary donors (D18, D18-Cl, and PBT1-C-2Cl) under the illumination of AM 1.5 G, 100 mW/cm^2.

Donor 1	Donor 2	Acceptor	V_{oc}^{a} (V)	J_{sc}^{a} (mA cm^{-2})	FF^a (%)	PCE^a (%)
PM6	-	Y6^{b,d}	0.832 (0.831 ± 0.001)	26.1 (25.8 ± 0.3)	77.6 (77.2 ± 0.4)	16.9 (16.6 ± 0.2)
PM6	-	L8-BO^{b,e}	0.888 (0.888 ± 0.001)	25.7 (25.5 ± 0.3)	79.9 (79.5 ± 1.1)	18.2 (18.0 ± 0.1)
PM6	D18	Y6^{c,d}	0.839 (0.838 ± 0.001)	26.7 (26.4 ± 0.2)	79.1 (79.1 ± 0.4)	17.7 (17.5 ± 0.2)
PM6	D18-Cl	Y6^{c,d}	0.844 (0.843 ± 0.002)	27.0 (27.0 ± 0.2)	77.8 (77.3 ± 0.7)	17.8 (17.6 ± 0.1)
PM6	PBT1-C-2Cl	Y6^{c,d}	0.834 (0.832 ± 0.002)	26.8 (26.8 ± 0.3)	78.2 (77.4 ± 0.6)	17.5 (17.3 ± 0.1)
PM6	D18	L8-BO^{c,e}	0.896 (0.896 ± 0.001)	26.7 (26.6 ± 0.3)	81.9 (81.1 ± 0.8)	19.6 (19.3 ± 0.1)
PM6	D18-Cl	L8-BO^{c,e}	0.897 (0.897 ± 0.002)	26.4 (26.4 ± 0.2)	80.8 (80.0 ± 0.8)	19.1 (18.9 ± 0.1)
PM6	PBT1-C-2Cl	L8-BO^{c,e}	0.890 (0.890 ± 0.001)	26.2 (26.2 ± 0.2)	80.4 (79.6 ± 0.7)	18.7 (18.6 ± 0.1)

[a]The average values are obtained from 20 devices, with an aperture area of 3.2 mm^2. The values outside the parentheses denote the best optimal photovoltaic parameters, and the values inside the parentheses represent the average photovoltaic parameters and their standard deviations. [b]D:A=1:1.2 (weight ratio); [c]D1:D2:A=0.8:0.2:1.2 (weight ratio). [d]The device architecture is ITO/PEDOT:PSS/active layer/PNDIT-F3N/Ag; donor concentration = 6.5 mg mL^{-1} in CF with 0.5% 1-CN, following with 85 °C TA treatment for 5 min. [e]The device architecture is ITO/PEDOT:PSS/active layer/PNDIT-F3N/Ag; donor concentration = 6.5 mg mL^{-1} in CF with DIB as a solid additive (the content of DIB is 50% of the total mass of donor and acceptor), following with 85 °C TA treatment for 5 min.

Supplementary Table 18. Photovoltaic parameters of OSCs under the illumination of AM 1.5 G, 100 mW/cm^2.

PM6:D18:L8-BO	V_{oc}^{a} (V)	J_{sc}^{a} (mA cm^{-2})	FF^a (%)	PCE^a (%)
1:0:1.2	0.888 (0.888 ± 0.001)	25.7 (25.5 ± 0.3)	79.9 (79.5 ± 1.1)	18.2 (18.0 ± 0.1)
0.8:0.2:1.2	0.896 (0.896 ± 0.001)	26.7 (26.6 ± 0.3)	81.9 (81.1 ± 0.8)	19.6 (19.3 ± 0.1)
0.5:0.5:1.2	0.901 (0.901 ± 0.001)	25.5 (25.2 ± 0.3)	79.4 (78.9 ± 0.8)	18.3 (18.0 ± 0.1)
0.2:0.8:1.2	0.903 (0.902 ± 0.001)	25.3 (24.9 ± 0.2)	78.8 (78.7 ± 0.6)	18.0 (17.7 ± 0.2)
0:1:1.2	0.907 (0.908 ± 0.001)	24.9 (24.3 ± 0.5)	78.5 (78.5 ± 1.0)	17.7 (17.4 ± 0.2)

[a] The average parameters were calculated from 50 devices.

Supplementary Table 19. The carrier mobility, lifetime, and diffusion length of the device under different blend ratios, as well as the lifetime of the hole transfer process in different blend films.

PM6:D18:L8-BO	μ_e [a] ($cm^2 V^{-1} s^{-1}$)	μ_h [a] ($cm^2 V^{-1} s^{-1}$)	τ_c (s)	L_e (nm)	L_h (nm)	τ_1 (ps)	τ_2 (ps)
1:0:1.2	$(1.50 \pm 0.12) \times 10^{-3}$	$(1.15 \pm 0.12) \times 10^{-3}$	1.87×10^{-6}	85 ± 3.3	75 ± 3.5	0.46	16.61
0.8:0.2:1.2	$(1.49 \pm 0.12) \times 10^{-3}$	$(1.42 \pm 0.13) \times 10^{-3}$	2.88×10^{-6}	106 ± 3.6	103 ± 4.0	0.51	18.17
0.5:0.5:1.2	$(1.43 \pm 0.12) \times 10^{-3}$	$(1.54 \pm 0.11) \times 10^{-3}$	1.62×10^{-6}	78 ± 2.4	81 ± 1.8	0.53	18.33
0.2:0.8:1.2	$(1.47 \pm 0.12) \times 10^{-3}$	$(1.59 \pm 0.10) \times 10^{-3}$	1.13×10^{-6}	66 ± 2.5	68 ± 1.8	0.63	18.92
0:1:1.2	$(1.40 \pm 0.11) \times 10^{-3}$	$(1.80 \pm 0.10) \times 10^{-3}$	1.01×10^{-6}	61 ± 2.3	69 ± 1.9	0.74	19.30

[a] The average parameters were calculated from 5 devices.

Supplementary Table 20. Morphological characteristic parameters of different blend films.

PM6:D18:L8-BO	Center to center distance (CCD, nm)	Fibril diameter (FD, nm)	Mixing region size (MRS, nm)[a]
1:0:1.2	47.8	14.3	9.6
0.8:0.2:1.2	48.2	19.1	5.0
0.5:0.5:1.2	58.1	19.6	9.5
0.2:0.8:1.2	60.6	18.1	12.2
0:1:1.2	64.1	17.1	15.0

[a] $\mathrm{MRS} = \frac{\mathrm{CCD} - 2\mathrm{FD}}{2}$

Supplementary Table 21. The carrier mobility, lifetime, and diffusion length of the device under different conditions, as well as the lifetime of the hole transfer process in different blend films.

Blends	μ_e [a] (cm^2 V^{-1} s^{-1})	μ_h [a] (cm^2 V^{-1} s^{-1})	τ_c (s)	L_e (nm)	L_h (nm)	τ_1 (ps)	τ_2 (ps)
PM6:Y6 (1:1.2)	(1.23 ± 0.09) × 10^{-3}	(1.18 ± 0.10) × 10^{-3}	1.65 × 10^{-6}	73 ± 2.5	71 ± 2.9	0.73	19.84
PM6:D18:Y6 (0.8:0.2:1.2)	(1.57 ± 0.11) × 10^{-3}	(1.42 ± 0.09) × 10^{-3}	2.07 × 10^{-6}	92 ± 2.9	87 ± 2.6	0.56	18.35
PM7:L8-BO (1:1.2)	(1.14 ± 0.09) × 10^{-3}	(0.71 ± 0.13) × 10^{-3}	1.14 × 10^{-6}	58 ± 2.1	46 ± 4.1	0.66	19.31
PM7:D18:L8-BO (0.8:0.2:1.2)	(1.49 ± 0.11) × 10^{-3}	(1.48 ± 0.08) × 10^{-3}	1.63 × 10^{-6}	80 ± 2.8	79 ± 2.0	0.67	18.97
PTQ10:L8-BO (1:1.2)	(1.31 ± 0.12) × 10^{-3}	(0.84 ± 0.11) × 10^{-3}	9.21 × 10^{-7}	56 ± 2.4	45 ± 2.9	0.58	19.37
PTQ10:D18:L8-BO (0.8:0.2:1.2)	(1.52 ± 0.09) × 10^{-3}	(1.57 ± 0.12) × 10^{-3}	1.43 × 10^{-6}	75 ± 2.2	76 ± 3.3	0.62	19.21

[a] The average parameters were calculated from 5 devices.

Supplementary Notes

Supplementary Note 1. Analysis of TPC, TPV, and Mott-Schottky measurements

The TPV and transient photocurrent (TPC) measurements were used to study the recombination mechanism[9]. The charge density in devices is determined by the differential capacitance method as shown in Supplementary Fig. 26b. A clear exponential dependence on V_{oc} is demonstrated. Following $n = n_0 e^{\gamma V_{\mathrm{oc}}}$, where n_0 is the average charge density in the active layer in dark conditions, the derived charge lifetime versus charge density is shown in Supplementary Fig. 26c. In this case, a power-law dependence indicates that the non-geminate/free charge recombination is the major loss mechanism under open-circuit condition. Fig. 3c shows the relationship between the non-geminate recombination rate coefficient and charge density, and the ternary device exhibits a lower recombination coefficient under the same charge density. Supplementary Fig. 27 shows the defects density of state (DoS) and the built-in potential measured following the Mott-Schottky method[10]. The DoS in the ternary mixture decreases compared to that of PM6:L8-BO blends, yet higher than that of D18:L8-BO blends. To further understand the potential role of trap states, impedance spectroscopy (IS) was conducted to access the occupied LUMO DoS, which is a method to probe the density of photo-generated charges (N) as a function of light intensity (or Fermi level) up until 1 sun equivalent condition (shown in Supplementary Fig. 28). The LUMO DoS and related parameters derived from the capacitance spectra are summarized in Fig. 3d and Supplementary Table 11. While no clear difference in terms of δ (the energetic disorder parameter), the PM6:D18:L8-BO device shows a larger N value, correlating well with the J_{sc} improvement. Moreover, the device based on D18:L8-BO shows a large β/α (calculated from the slope in Supplementary Fig. 29) of 2.8 indicates more trapped carrier recombination, and the addition of PM6 could suppress this recombination with a smaller β/α of 2.31. A similar conclusion can be drawn from the relative values of estimated trap density ($U_{\mathrm{n,p}}^{\mathrm{Gau}}$) and N, where the PM6:D18:L8-BO device shows the smallest $U_{\mathrm{n,p}}^{\mathrm{Gau}} / N$ value (shown in Supplementary Table 11). However, as the ratio between trapped and N is very small ($<10^{-3}$), trap-assisted recombination is believed to be negligible as opposed to bimolecular recombination in all three devices, which is also evidenced in the slope of SCLC characteristics,[11] where all three devices show the maximum slope of ~2 (see Supplementary Fig. 25).

Supplementary Note 2. Coupled exciton diffusion, optical transfer matrix, and drift diffusion modelling

The experimental results have shown that the double fibril network facilitated efficient exciton diffusion and lower recombination are two primary reasons for the improved performance from binary to ternary blends. To further support this claim, we here perform device modelling to quantitatively investigate the effect of exciton diffusion and recombination on electrical and optical response of the photovoltaic devices to the changes of photoactive layer properties. Specifically, the effects of exciton diffusion efficiency and free charge recombination rate constant on IQE/EQE, J_{sc}, and FF are modelled using experimental parameters as inputs. Our simulations start with estimating the exciton diffusion efficiency, followed by optical modelling based on a transfer matrix method, and end by the solution of the charge carrier continuity, transport, and Poisson's equation to account for electrostatic effects.

Estimating exciton diffusion efficiency with acceptor domains:

The experimental results show that the exciton decay rate, diffusion length, and domain size are different from blend to blend (Supplementary Table 12). Thus, one would expect a different fraction of excitons to reach the edge of the domains and split to become free charges. To model this process, we imagine the acceptor L8-BO (i.e. the primary absorber domain) to be a simple 3D sphere with a uniform photogeneration profile (see Supplementary Fig. 30). We assume the only loss of excitons within the domain is through direct decay (i.e. through exciton lifetime τ). And the dissociation of excitons is only allowed at the edge or outside of the sphere, with a dissociation rate depending on the blends (k_{diss}). Note here that in all devices, k_{diss} is in the scale of ps^{-1}, indicating ultrafast dissociation of exciton at donor/acceptor interfaces in all devices, therefore, the key difference here is the size of acceptor domains. The detailed parameters for exciton diffusion modelling are taken from experimental values as summarized in Supplementary Table 12. As such, the exciton diffusion process is governed by the formula below:

$$0 = \nabla D \nabla X(r) + G(r) - \frac{X(r)}{\tau} - k_{\text{diss}}(r) X(r)$$

Where, $X(r)$ is the density of exciton as a function of position (r), D is the diffusion coefficient, $G(r)$ is the exciton generation rate, τ is the lifetime of excitons in absence of quencher, and $k_{\text{diss}}(r)$ is the dissociation rate constant from exciton to free charges. $k_{\text{diss}}(r)$ is zero inside and non-zero outside the sphere. The solution of exciton diffusion equation provides the total loss inside the sphere ($\iiint \frac{X(r)}{\tau} \mathrm{d}V$, $\mathrm{d}V$ is the integral volume), and the exciton diffusion efficiency (P_{diss}) is then calculated via

$$P_{\mathrm{diss}} = 1 - \iiint \frac{X(r)}{\tau} \mathrm{d}V \Big/ \iiint G(r) \mathrm{d}V$$

Using the data from Supplementary Table 12 (i.e. diffusion constant, diffusion length, dissociation rate, and phase separation scales), we obtain values of P_{diss} by solving exciton diffusion equations. The resulting values are 93.74%, 96.87%, and 96.64% for D18:L8-BO, PM6:L8-BO, and PM6:D18:L8-BO, respectively. Clearly, PM6:D18:L8-BO and PM6:L8-BO devices show higher exciton diffusion efficiency than D18:L8-BO devices. And no clear difference between PM6:D18:L8-BO and PM6:L8-BO device is seen, which is likely because that i) exciton diffusion in polymer domains is omitted, and ii) variations of exciton diffusion parameters in complex blends cannot be considered in the single domain simulations. We consider the accurate simulation of exciton diffusion process in both polymer and acceptor domains with different sizes is challenging and beyond the scope of this work. Nevertheless, we acknowledge the fact that the difference between PM6:D18:L8-BO and PM6:L8-BO in experimental IQE/EQE is also much smaller than that between PM6:D18:L8-BO and D18:L8-BO, as shown in Supplementary Fig. 7, which to some extent agrees with the simulations results above.

Calculation of quantum efficiencies, current-voltage characteristics, and fill factor:

Using the calculated P_{diss}, we then performed optical and electrical modelling. The optical modelling was conducted using experimental complex refractive index data obtained by ellipsometry measurements. The refractive index data for active layers are shown in Supplementary Fig. 31. The refractive index data of ITO, PEDOT:PSS, and Ag were taken from previously published works[12], and for simplicity, the transparent interlayer PNDIT-F3N was omitted since it's only 5 nm thick. For drift diffusion modelling, the charge generation rate was calculated using coupled exciton diffusion and optical models. And most of the input parameters were obtained from experimental measurements, except for dielectric constant (set at 3), effective density of state of free charges (set at 1×10^{26} m^{-3}),[1] and the injection barriers for cathode and anode are set to be close to zero. Since trap-assisted recombination is believed to be negligible in all devices as discussed in the main text, the most important parameter here is then the free-to-free recombination rate coefficient (B_{dir}), i.e. bimolecular recombination rate coefficient, which follows experimental values obtained using TPV/TPC. The detailed parameters for drift diffusion modelling are shown in Supplementary Table 13.

Supplementary Fig. 32a shows the simulated IQE and EQE using the coupled exciton diffusion, optical and electrical model with AM1.5G solar spectrum. IQE and EQE show a very similar trend as experimental results in Supplementary Fig. 7 when changing the blend, indicating that external parameters, such as reflection and transmission, are not the limiting factors here, agreeing with experimental observations. Moreover, in the wavelength range between 600 and 800 nm, the simulated IQE/EQE of the ternary device is about 5% higher than D18:L8-BO device, and the values for PM6:L8-BO device are similar to the ternary device. Overall, the ternary device shows the highest IQE/EQE, which confirms the highest photocurrent. Further current-voltage simulation (Supplementary Fig. 32b) demonstrates the highest J_{sc} in the ternary device (~24.6 mA cm^{-2}), followed by PM6:L8-BO (~24.0 mA cm^{-2}) and D18:L8-BO (~23.1 mA cm^{-2}). Although the exact values do not perfectly match the experimental values of J_{sc} in Supplementary Fig. 32b, we note that the trend has been successfully reproduced. The possible reasons for non-perfect match with experiments could be i) exciton diffusion in polymer domains is omitted, and ii) variations of exciton diffusion parameters in complex blends cannot be considered in the single domain simulations. We consider the accurate simulation of exciton diffusion process in both polymer and acceptor domains with different sizes is challenging and beyond the scope of this work.

We further analyzed the fill factors (FFs) using drift diffusion modelling. The calculated FFs reflect well the differences in device parameters, especially the B_{dir}, where the ternary device again shows the lowest B_{dir} experimentally, and correspondingly the highest FF, as shown in Supplementary Fig. 32c. We have also shown in Supplementary Fig. 32c the effect of direct recombination coefficient on FF in the studied devices, a strong connection between FF and B_{dir} is observed. The correlation between FF and recombination rate coefficient can also be investigated via a figure-of-merit quantifying the competition between charge recombination and transport, i.e. $\alpha = \sqrt{\frac{qB_{\mathrm{dir}}L^3J_{\mathrm{ph}}}{4\mu_{\mathrm{e}}\mu_{\mathrm{h}}(k_{\mathrm{B}}T)^2}}$, where q is the elementary charge, k_{B} is the Boltzmann constant, L is the active layer thickness, J_{ph} is the photogenerated current density under 1 sun.[6] Since the mobilities are rather similar among the three devices, the recombination rate coefficient should be the dominating factor, and the results show that PM6:D18:L8-BO possesses the lowest α (0.76), while the values for PM6:L8-BO and D18:L8-BO are 1.02 and 1.74, respectively. The analysis on α here therefore agrees with the coupled optical and electrical model results. And the devices studied here lie closely on the border between Shockley-type and transport limited regime following the guideline suggested in reference[6] (see also Supplementary Fig. 32d).

Overall, the coupled exciton diffusion, transfer matrix, and drift-diffusion model simulations above show decent agreements with our experimental results despite of the simplicity, and further support the claim that enhanced exciton diffusion and reduced free charge recombination are important reasons for the performance enhancement in the ternary device.

Supplementary References

1 MacKenzie, R. C. I., Shuttle, C. G., Chabinyc, M. L. & Nelson, J. Extracting Microscopic Device Parameters from Transient Photocurrent Measurements of P3HT:PCBM Solar Cells. *Adv. Energy Mater.* **2**, 662-669, (2012).

2 Xiao, B. *et al.* Relationship between Fill Factor and Light Intensity in Solar Cells Based on Organic Disordered Semiconductors: The Role of Tail States. *Phys. Rev. Appl.* **14**, 024034, (2020).

3 Wood, S., Blakesley, J. C. & Castro, F. A. Assessing the Validity of Transient Photovoltage Measurements and Analysis for Organic Solar Cells. *Phys. Rev. Appl.* **10**, 024038, (2018).

4 Chandrabose, S. *et al.* High Exciton Diffusion Coefficients in Fused Ring Electron Acceptor Films. *J. Am. Chem. Soc.* **141**, 6922-6929, (2019).

5 Cha, H. *et al.* Exciton and Charge Carrier Dynamics in Highly Crystalline PTQ10:IDIC Organic Solar Cells. *Adv. Energy Mater.* **10**, 2001149, (2020).

6 Neher, D., Kniepert, J., Elimelech, A. & Koster, L. J. A. A New Figure of Merit for Organic Solar Cells with Transport-limited Photocurrents. *Sci. Rep.* **6**, 24861, (2016).

7 Cook, S., Furube, A., Katoh, R. & Han, L. Estimate of singlet diffusion lengths in PCBM films by time-resolved emission studies. *Chem. Phys. Lett.* **478**, 33-36, (2009).

8 Hedley, G. J. *et al.* Determining the optimum morphology in high-performance polymer-fullerene organic photovoltaic cells. *Nat. Commun.* **4**, 2867, (2013).

9 Foertig, A., Baumann, A., Rauh, D., Dyakonov, V. & Deibel, C. Charge carrier concentration and temperature dependent recombination in polymer-fullerene solar cells. *Appl. Phys. Lett.* **95**, 052104, (2009).

10 Khelifi, S. *et al.* Investigation of defects by admittance spectroscopy measurements in poly (3-hexylthiophene):(6,6)-phenyl C61-butyric acid methyl ester organic solar cells degraded under air exposure. *J. Appl. Phys.* **110**, 094509, (2011).

11 Röhr, J. A., Shi, X., Haque, S. A., Kirchartz, T. & Nelson, J. Charge Transport in Spiro-OMeTAD Investigated through Space-Charge-Limited Current Measurements. *Phys. Rev. Appl.* **9**, 044017, (2018).

12 Dennler, G. *et al.* Angle dependence of external and internal quantum efficiencies in bulk-heterojunction organic solar cells. *J. Appl. Phys.* **102**, 054516, (2007).